Integration of fluorescence and atomic force microscopy for single molecule studies of protein complexes

Diplomarbeit im Fach Physik

von

David Fronczek

Julius-Maximilians-Universität Würzburg

Lehrstuhl für Experimentelle Physik V
Prof. Dr. B. Hecht

—

Rudolf-Virchow-Zentrum,
DFG-Forschungszentrum für Experimentelle Biomedizin
Dr. I. Teßmer

Oktober 2009

Zusammenfassung. Im Rahmen dieser Arbeit wurde ein bildgebendes Verfahren zur Identifizierung einzelner Proteine in rasterkraftmikroskopischen Aufnahmen entwickelt. Dazu wird ein integrierter Versuchsaufbau aus einem Rasterkraft- und einem optischen Mikroskop verwendet. Ziel der Technik ist die Identifizierung einzelner Proteine im biologischen Kontext (z. B. in Proteinkomplexen). Dazu werden ausgewählte Proteine fluoreszierend markiert und parallel zur Rasterkraftmessung optisch abgebildet. Für dieses Verfahren werden transparente und zugleich nano-glatte Substrate benötigt. Dazu wurden Probenträger aus Glas und Mica (Muskovit) verwendet und evaluiert. Als Fluoreszenzfarbstoffe kommen Quantenpunkte zum Einsatz, bestehend aus 5–10 nm großen Nanokristallen, die vermittels Antikörper stabil an Proteine gebunden werden können, ohne deren Funktion zu beeinträchtigen. Die optische Anregung erfolgt durch einen Argon-Laser, unter Verwendung des Prinzips der Totalreflektions-Fluoreszenz-Mikroskopie (TIRF). Im optischen Bild erscheinen die Fluorophore als einzelne Beugungsscheibchen. Durch eine Ausgleichsrechnung, bei der eine 2D-Gaußfunktion an die Daten angepasst wird, werden die Positionen der Fluorophore mit hoher Genauigkeit ermittelt (Superlocalization). Anschließend werden die Bilder durch eine affine Transformation ausgerichtet. Diese Transformation wird durch ein merkmalbasiertes Bildregistrierungsverfahren numerisch bestimmt, welches die Koordinaten einiger identischer Punkte in den Rasterkraft- und Fluoreszenzbildern als Eingabe benötigt. Die Programmierung und Evaluierung des zur Auswertung erforderlichen Algorithmus war Teil der Arbeit. Die Positionen der Fluorophore werden anschließend farbkodiert im topografischen Bild ausgegeben, was die Identifizierung einzelner Proteine/Objekte ermöglicht. Zur experimentellen Realisierung des Verfahrens wurden Abbildungen mit ungebundenen Quantenpunkten erstellt, wobei eine Überlagerungsgenauigkeit von $\sim 6\,\mathrm{nm}$ (Glas) bzw. $\sim 9\,\mathrm{nm}$ (Mica) erreicht werden konnte. Ergänzend dazu wurden Simulationen durchgeführt, um die Validität des Auswertungsalgorithmus zu bestätigen. Diese ermöglichen zusätzlich Vorhersagen über die zu erwartende Genauigkeit unter verschiedenen Abbildungsbedingungen. Schließlich wurde die Technik exemplarisch auf ein biologisches System angewendet. Dazu wurde der Schadenserkennungsapparat des bakteriellen DNS-Reparatursystems NER herangezogen. Bei gleichzeitig deutlicher Sichtbarkeit einzelner DNS-Moleküle und Proteine im Topographiebild konnte eine Überlagerungsgenauigkeit von 8.8 nm erreicht werden.

Contents

1. Introduction

The aim of this work is to develop a novel single-molecule imaging technique by combining atomic force microscopy and optical fluorescence microscopy. To identify single proteins in a topographical image, they are labelled with fluorescent dyes and the positions of these fluorophores are determined with high precision in an optical image. The two images are then aligned and the positions of the fluorophores are displayed on top of the topographical data.

With the invention of atomic force microscopy (AFM) in 1986, Binning, Quate and Gerber [1] expanded the application of high resolution scanning probe microscopy to the study of insulating materials and thus made it available for biological samples. AFM generates a topographical map of a specimen by sampling the interaction forces between its surface and a pointed tip on a flexible cantilever. The benefits of this imaging technique include high contrast without the need for staining and nanometre lateral resolution under ambient conditions [2]. Consequently, the popularity of AFM in the field of cellular and molecular biology has steadily increased [3]. However, features that are roughly similar in size and stiffness cannot be told apart by AFM alone. Biological samples, made up of proteins, often fall in that category. Even in high resolution images, the inner structure of a protein does not provide enough information to doubtlessly identify a particular type of protein. Additionally, many proteins can form complexes with each other or with other macromolecules present in the cell, e .g. DNA. Thus, for many biological issues not only molecular resolution is required, but it is desirable — if not crucial — to know exactly what proteins are involved in a specific complex [4] or what their relative positions are.

On the other hand, fluorescence microscopy is one of the most common and important research techniques in the life sciences [5]. In contrast to AFM it most notably provides a high time resolution [6] and allows for multi-colour labelling by means of the "fluorescent toolbox", as Giepmans et al. [7] called their review of fluorescent dyes that can be attached to single proteins. It suffers from two principle limitations, though. Firstly, only the fluorescent molecules are detectable by this

technique, of course. Secondly, the resolution is determined by the diffraction limit, which is typically two orders of magnitude larger than the size of a single protein. Many ideas to circumvent or overcome the second limitation exist, including SNOM [8, 9], STED [10] and PALM [11]. An especially interesting approach was realized by Yildiz et al. [12, 13] in 2003. Based on the works of Bobroff [14] and Thompson et al. [15], Yildiz et al. localize a single fluorophore with a nanometre resolution by fitting a 2D-Gaussian function to its diffraction limited spot. The term superlocalization or "Fluorescence Imaging with One Nanometre Accuracy" (FIONA) was coined for that technique. In the original publication, this method was used to track the positions of the fluorophores over time. However, it is also possible to use the positions computed with high precision to exactly register the optical image to an AFM image of the same area. In this work such an integrated imaging technique was developed by attaching semiconductor nanocrystal quantum dots to single proteins [16], depositing them on a transparent substrate and recording both the topography and fluorescence of the same sample region. The quantum dots are visible in both the AFM and optical images and can thus serve as fiducial markers for the registration. When the two independently acquired images are aligned, the FIONA algorithm is applied to the fluorescent labels in the optical image. Finally, the fitted positions of the fluorophores are displayed with high accuracy on top of the AFM data, resulting in a high spatial resolution of the whole topography, with individual molecules specifically labelled.

Outline. This document is structured in six chapters. Following this introduction, the experimental techniques of AFM and single molecule fluorescence microscopy are described in chapter 2, along with the theoretical foundations and the data analysis techniques used, including superlocalization. Then, the problem of finding samples and, especially, substrates suitable for both optical and AFM imaging is discussed in chapter 3. Next, the task of image alignment or — how it is often called in a biological or medical setting — image registration is explained and carried out for two showcase images in chapter 4. Sources of errors and the accuracy achieved are also discussed in this section together with the mathematical background. A biological application is presented in chapter 5, illustrating the utilization of the method. Finally, potential improvements and extensions of the technique are depicted in the outlook.

2. Basics

A sketch of the experimental setup is shown in Fig. 1. A photograph of the setup can be seen in Fig. 5 on page 13. In the following sections the main components of the system are described in detail along with the necessary theoretical background.
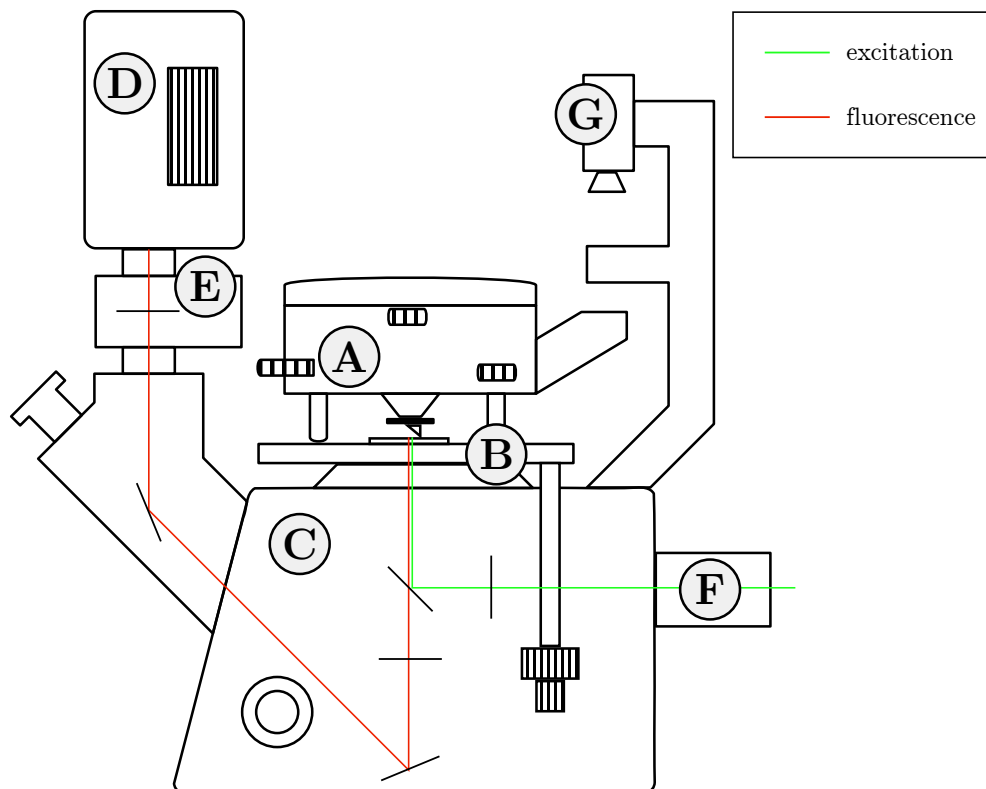

Fig. 1: Sketch of the experimental setup. The labels denote: **A** AFM scan head; **B** Scanning stage with sample holder; **C** Inverted optical microscope; **D** EMCCD camera; **E** external $1-4\times$ magnification lens; **F** TIRF unit, laser incoupling; **G** Top view camera and back light. The optical components are described in Fig. 7 on page 18.

2.1. Atomic force microscopy

2.1.1. Introduction & theory

The atomic force microscope belongs to the family of high resolution scanning probe microscopes, a branch of microscopy founded by Binning and Rohrer with the development of the scanning tunnelling microscope (STM) in 1981 (Nobel prize 1986, see [17]). It moves a small probe tip over a surface making measurements of the tunnel current through the tip at regular intervals. These single data points will then be compiled to a comprehensive map of the surface. Highly precise positioning systems are needed for the scanning, typically realized by piezoelectric actuators. In the case of the STM, the measured quantity is related to the surface's conductivity, which has to be sufficiently high for the STM to perform well. Therefore its application to biological samples is difficult, albeit possible [18], and the STM was not widely used in the field of life sciences. This situation changed when the STM setup was modified to control and measure the z-deflection of the microscope tip by other means than the tunnel current. The atomic force microscope (AFM) is controlled by the forces arising between atoms in close contact. The tip stands on the end of a flexible cantilever, whose deflection due to the forces between the tip and the surface is measured. A discussion of the forces involved can be found in the detailed AFM review of Seo et al. [2].

Different modes of operation exist, separated in static and dynamic modes, the latter being either frequency or amplitude modulated and in the regime of attractive or repulsive forces, compare p. 18ff in [19]. Frequency modulated non-contact mode is superior by design, see p. 22f in [19], and is nowadays almost exclusively used for atomic resolution experiments in vacuum. However, it has some practical drawbacks, especially when imaging under ambient conditions [20], therefore amplitude modulated intermittent-contact mode is used for this work. In this mode, often called "tapping", strong repulsive forces can be taken advantage of, making the measurement less susceptible to noise. Additionally, it is comparatively easy to stabilize the instrument in this mode, since the high amplitude used prevents disturbances common in other dynamic modes, e. g. snap-to-contact.

Most current atomic force microscopes detect the oscillation of the cantilever optically by monitoring the deflection of a beam reflected on the back of the cantilever. The light source can be a laser or — as is the case with the instrument used for this work — a super-luminescent diode (IR-SLD).

A common figure of merit for the quality of the images obtained by AFM is the surface roughness, given by

$$\varrho = \sqrt{\frac{1}{N_p} \cdot \sum_i z_i^2} \, , \qquad (1)$$

where i runs over all N_p pixels, cf. [21]. Both the physical roughness of the surface and noise contribute to ϱ. For surfaces with a known roughness, ϱ can be used to estimate the amount of noise present and hence the stability of the imaging process. Another figure of interest is the image resolution. While the detection of the z-deflection is very sensitive and practically only limited by ambient noise [1, 2], the lateral resolution depends largely on the imaging parameters chosen. Of course, it can't be better than the nominal pixel resolution r_A, but other limitations for the x- and y-resolution are given by the step size of the positioning system and, most notably, by the sharpness of the probe, i.e. the bending radius at its tip, compare p. 188f in [19]. Furthermore, a trade-off exists between imaging time and resolution. The time required for acquisition is roughly proportional to the number of single measurements to be conducted, i.e. the total number of pixels. If the scanning speed is chosen too high or the pixel size too small, the actual resolution of the image will be lower than its nominal pixel resolution r_A indicates. If, on the other hand, the pixel size is chosen too large, small features lying in between two adjacent scanning rows will not be noticed. What imaging conditions should be chosen for a particular experiment must be decided for each individual case, taking the above considerations into account.

2.1.2. Instrumentation

The whole system (including the optical microscope) is installed on top of an active vibration isolation table (*MOD-1 plus*, Halcyonics, Göttingen, Germany) and in an acoustic enclosure (*BCH-45*, Technical Manufacturing Corporation (TMC), Peabody, MA, USA) to avoid the incoupling of ambient noise and vibrations. A photograph of the setup with the enclosure open can be seen in Fig. 5.

The *MFP-3D* atomic force microscope (Asylum Research, Santa Babara, CA, USA), used for this work, is a versatile imaging system, allowing for all common types of AFM measurements in air and in liquid. The instrument consists of three parts: The actual AFM head, a controller unit and a standard PC.

The AFM head is shown in Fig. 2. It contains the tip holder, the z-piezo and
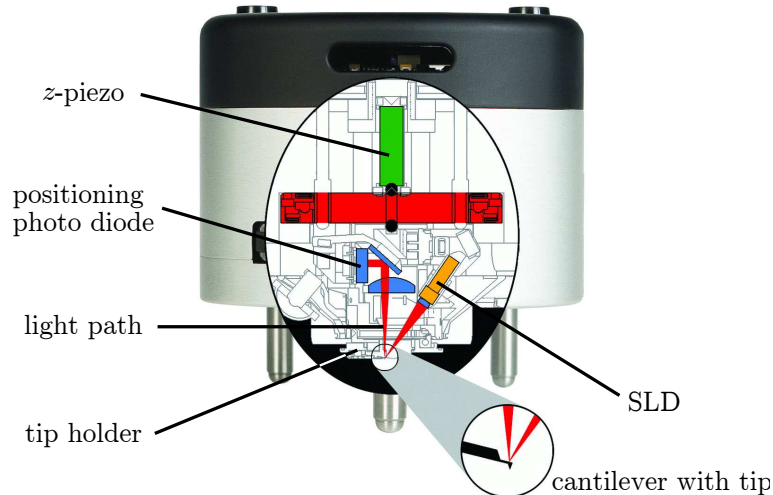
Fig. 2: Diagram of the *MFP-3D* AFM head. With permission of Asylum Research.

the so-called shake-piezo, which is responsible for the mechanical excitation of the tip in AC-mode. It has some built-in amplifiers and analog-to-digital converters (ADCs) to avoid the transportation of weak analog signals along external cables. The optical deflection detection is completely included in the head, too. It operates at a wavelength of 860 nm, far away from the fluorescence, hence stray light can be easily filtered out. The position of the detection diode and the laser orientation can be controlled manually by three hand wheels on the outside of the AFM head. A fourth wheel moves the whole head up and down the z-direction and is used to bring the tip in close contact with the sample before engaging. The AFM head does not move the tip in x- and y-, but only in z-direction. The lateral movement is instead performed by the sample stage, which is mounted on top of the optical stage. Its positioning system is stabilized by a closed-loop feedback system using capacitive sensors, resulting in drift-free position control.

The AFM controller is the interface between the high-level control exerted by the software and the requirements of the AFM head and scanning stage. Its tasks cover the analog-to-digital conversion of all signals not already converted by the AFM head's internal ADCs, driving the scanning stage and most of the low-level digital signal processing, i e. tuning, frequency filtering, echo-suppression, etc.

The experiment is controlled by the *MFP-3D* software, based on *IGOR Pro 6* (Wavemetrics, Portland, OR, USA). A screenshot of the user interface is shown in Fig. 3. Most of the interface is self-explanatory; in the "Master Panel" (A) the basic controls are found such as the scan area's size and offset, the scanning speed, drive and set-point amplitude, gains, etc. The "Channel Panel" (B) allows one to select
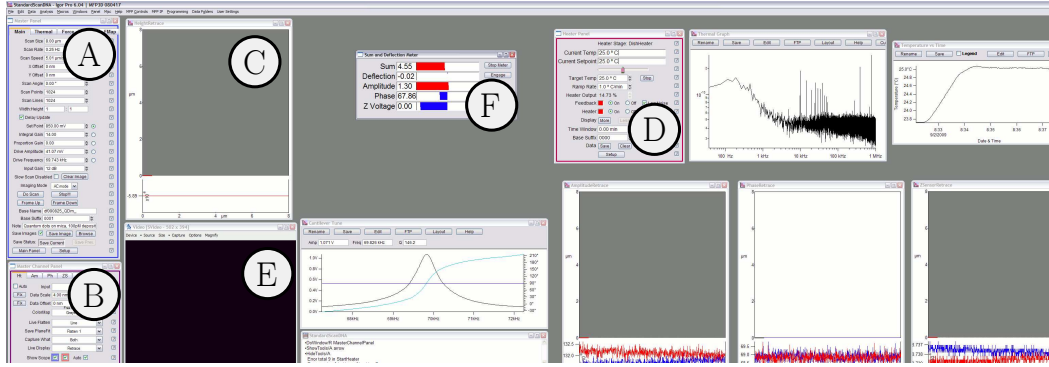
Fig. 3: Screenshot of the *MFP-3D* software's user interface. The Labels are: **A** Main scanning controls, **B** Display and capture controls, **C** Height map of the scanned area, **D** Stage heater controls, **E** Live video of the top view camera, **F** Live display of some important values.

different values for the live view (C) and storage, including basic image processing options, such as automatically correcting the offset, z-scale or slope of the scanned lines. The interface is completed by the heater control (D), a live picture of the auxiliary top view camera (E) and several status indicators, including a live metre showing some important values (the current diode signal, beam deflection, oscillation amplitude, phase and piezo extension) as bars (F).

For this work *AC240* SiN tips (*Micro Cantilever OMCL-AC240TSG-W2*, Olympus, Center Valley, PA, USA) were used. Their nominal drive frequency is $70\,\text{kHz}$, their spring constant $2\,\text{N/m}$ and they have a guaranteed tip radius of $\leq 10\,\text{nm}$.

First of all, the sample is attached to the scanning stage. A standard AFM sample holder can't be used, since the sample has to be accessible to the objective lens of the optical microscope from below. The sample is instead fixed directly on the stage by means of adhesive tape. The heater is then turned on to ensure a stable environment and to avoid thermal drift. Since there is no active cooling, the temperature setpoint is chosen a few degrees above room temperature in order to ensure that the controller, which adjusts the heating power, has a decent operating range. Next, the cantilever with the tip is installed into the AFM head and the beam of the deflection detection system is positioned on the free end of the cantilever with the help of the top view camera. In these experiments, the AFM is exclusively operated in tapping mode, meaning that the shake-piezo is used to excite the cantilever close to its resonance frequency, which has to be determined independently for each tip. The tuning is performed by constantly recording the amplitude while sweeping the frequency. When it is completed, a response curve of the tip is displayed, showing
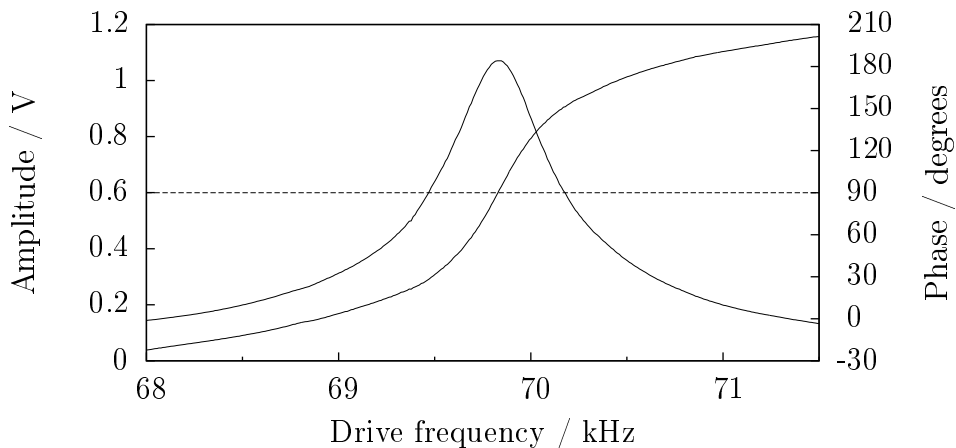
Fig. 4: A typical response curve for a make *AC240* cantilever.

both the amplitude of the oscillation and its phase against the drive frequency, cf. Fig. 4. Damage or contamination of the tip can be easily observed by looking at these curves. Tips with a very low or deformed resonance are discarded. The drive frequency is then chosen to be slightly (5–10 %) below the resonance frequency, which doesn't affect the amplitude much, but helps to keep the oscillation in repulsive mode, compare [2].

After the AFM head has subsequently been installed on top of the optical stage, the tip is brought in contact with the surface. In order to avoid damage to the tip, the z-piezo is fully extended and a set-point corresponding to a very weak tapping is chosen (typically 5 % below the free air amplitude). The tip is then moved down by the hand wheel on the AFM head until the z-piezo starts to retract. From this state, often called false engagement, the tip is brought into contact with the surface by decreasing the set-point only. During the false engagement, the extension of the z-piezo, i. e. the penetration of the layer of water and compressed air above the surface [20], follows the decreasing set-point. As soon as the tip is truly engaged, i. e. touching the surface, the z-piezo remains stable at a certain height. To ensure a comparable tapping force across multiple engagements and tips, the set-point is further lowered until the phase reaches a value 2° below the free air amplitude. This engagement procedure, also called "soft engage", is described in detail in [22].

The acoustic hood is then closed and the system is given a short time to equilibrate (5–15 min.), then the scanning process can begin. Settings for a typical scan are: proportional gain: 10–20; integral gain: 0; set-point: 850 mV ($= 85$ % of the free air amplitude); area: 16–256 μm^2, scanning speed: 2–5 μm/s, resolution: 2–8 nm/px,
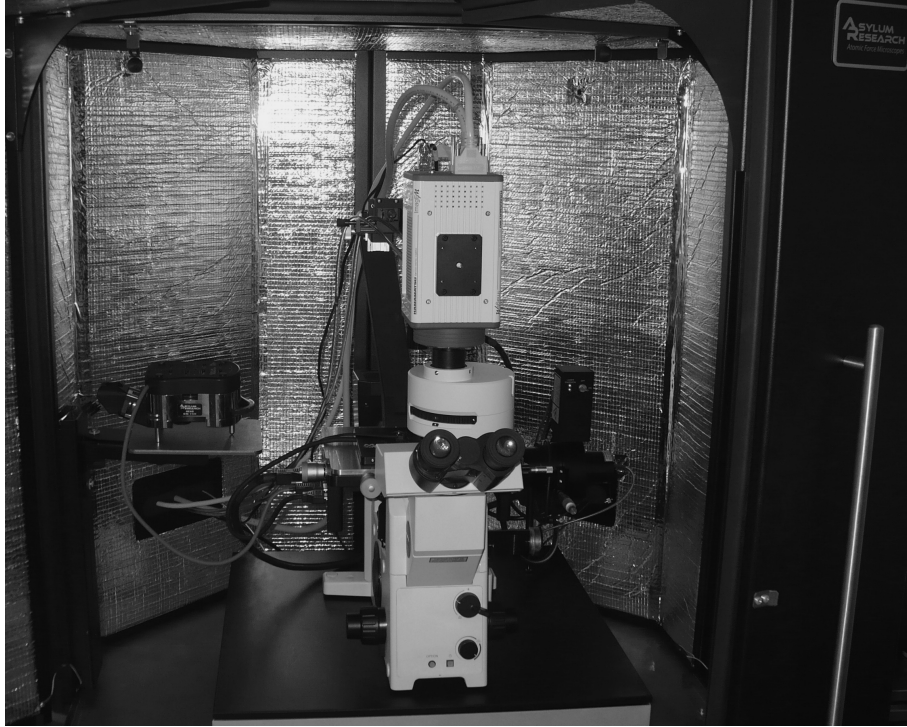
Fig. 5: Photo of the experimental setup.

corresponding to a total duration of 20–400 min for one scan. The data obtained is saved digitally in the form of raw *IGOR Pro binary wave* files.

2.1.3. Image analysis

The raw AFM data is processed using the *MFP-3D* software. First, images are "flattened", meaning that the average slope of each scan line is automatically adjusted to be zero. This is necessary, since neither the tip nor the sample can be installed 100 % horizontally. This procedure conserves absolute distances in the image and does not bias the data either way. Second, lines containing abnormally large amounts of noise are deleted from the image and replaced by the mean of the adjacent lines. Usually only a few lines (~ 1 %), selected by hand, are replaced in each image, their z-ranges are typically 10–100 times larger than those of the remaining lines. Even though information is removed during this step, it improves the quality of the images, because the data dropped does obviously not have its origin in topographical features of the sample. Third, the offset and z-scale of the data are adjusted to produce a good contrast without cutting off the highest features. Eventually, the images are exported as 8-bit greyscale TIFF files.

Some general information on the AFM images' quality can then be obtained: The

roughness ϱ can be determined using Eq. (1) and is readily computed by the *MFP-3D* software. Another important aspect is the cleanness of the sample, which can be judged by the eye or quantified by counting the number of visible features compared to the number of protein complexes or whatever be the object of interest.

Next, the positions of the fiducial markers are extracted from the data. For each, an area is selected in the image, containing the object to be used as a marker. These areas are referred to as regions of interest, or ROIs for short, as is customary in the field of image analysis. The position of the object is then determined by the analysis software (see Appendix A.3). The brightest pixel in each ROI is taken to be the centre of the object, while the mean uncertainty s_A is considered to be half the pixel size. Even though this algorithm may not provide the best resolution, it is robust, reproducible independent of noise and placement of the ROIs and very fast.

2.2. Optics

2.2.1. Theoretical foundations

Diffraction limit & point spread function. Conventional optical microscopy only exploits information from the far-field. Thus it suffers from a limitation of the resolution, arising from the fact that high spatial frequencies are not propagated to the far-field, see p. 45ff in [23].

Using light with a wavelength λ, all features smaller than

$$\Delta x \approx \frac{\lambda}{2} \tag{2}$$

will not be resolvable in the image, but appear as diffraction limited spots. The choice of wavelengths is restricted by the fact that biological samples such as proteins or DNA are excited and thereby damaged by photons with an energy above $\sim 4\,\mathrm{eV}$, corresponding to wavelengths smaller than $300\,\mathrm{nm}$ [24]. In this experiment, the fluorophore excitation occurs at $488\,\mathrm{nm}$, the emission at $605\,\mathrm{nm}$, resulting in a spot size $\geq 300\,\mathrm{nm}$. The same is true for spatially confined sources of light like single fluorophores. The focused image of a single emitter is described by the instrument's point spread function, see p. 89f in [23]. For optical experiments, this is typically an Airy disc, given by

$$a\left(x,y\right) = a_{max} \cdot \frac{J_1\left(s_a \cdot \sqrt{x^2 + y^2}\right)^2}{s_a^2 \cdot \left(x^2 + y^2\right)}, \tag{3}$$

where a_{max} and s_a are the height and width of the Airy function and $J_1(x)$ is the Bessel function of the first kind, first order, see p. 526ff, [25]. This function can be very well approximated by a 2D-Gaussian

$$g(x, y) = g_{max} \cdot \exp\left(\left(-\frac{x - x_0}{\sqrt{2} \cdot s_{g,x}}\right)^2 - \left(-\frac{y - y_0}{\sqrt{2} \cdot s_{g,y}}\right)^2\right) + g_0\,, \qquad (4)$$

where usually $s_{g,x} = s_{g,y} = s_g$ is the width of the function, g_{max} its height and (x_0, y_0) its centre. The additive term g_0 can be introduced to account for a possible background offset. However, this is only true for perfect optics. If not all light emitted by a single fluorophore can be focused on the same spot in the image plane, the patterns become more complex, compare p. 779f in [5]. Focusing and emission near planar interfaces are discussed in detail in [23], see p. 73–86 and 335–360 therein. It had been shown by Cheezum et al. [26] that in most cases a 2D-Gaussian is nevertheless the most suitable approximation for localizing a single emitter.

SNR. The signal to noise ratio or SNR generally is a measure of the quality of the signal and thus a limit for the information that can be obtained from a measurement. Depending on the measured quantity and type of noise, an appropriate method of calculating the SNR has to be chosen. In the present case the noise is dominated by the shot noise, inherent to the process of photon detection. The shot noise alone is governed by a Poissonian noise distribution,

$$\text{SNR} = \frac{N}{\sqrt{N}} = \sqrt{N}\,, \qquad (5)$$

resulting in a SNR proportional to the square root of the number of collected photons $\sqrt{N}$. Other sources of noise are the background noise, induced e.g. by scattered light, and the readout noise of the detector [27]. They both induce a constant level of noise [28], independent of the signal height and therefore contribute more strongly if very few photons are collected. All other contributions to the noise, including the dark current of the detector, are small in comparison and thus neglected. A conservative, all-inclusive approach, advocated by Cheezum et al. [26], is given by

$$\text{SNR} = \left(\frac{\zeta_{max} - b}{\sqrt{\zeta_{max} + b}}\right)\,. \qquad (6)$$

Here ζ_{max} is the height of a fluorescent peak (or the mean height of many) and b is the mean rms background, whose fluctuations are assumed to be $\sqrt{b}$. This approach

separates the SNR into two regimes: One governed by the background, the other one governed by the shot noise.

Total internal reflection fluorescence microscopy (TIRF). Some contributions to the noise scale with the detection volume, e.g. scattered fluorescence or Raman scatter from the substrate. It is therefore essential for single molecule detection to reduce this volume as far as possible, to obtain a high SNR despite the small signals, compare p. 757 in [5]. Using a TIRF setup [29], the detection volume can be confined to a fraction of the wavelength λ in z-direction. Total internal reflection occurs whenever a beam of light encounters a medium border coming from the side of the higher refractive index n_2 and the angle of incidence θ is larger than θ_c, the critical angle of total internal reflection:

$$\theta_c = \arcsin\left(\frac{n_1}{n_2}\right) ,$$

where $n_{1,2}$ are the refractive indexes of the distal and proximal medium. Only the evanescent field is used to excite the fluorophores located on top of the substrate, see Fig. 6. Another convenient effect of TIRF is the intensity enhancement at the interface. Depending on the polarization, the intensity of the evanescent field directly above the surface can be several times larger than the incoming intensity, see p. 33f in [23].
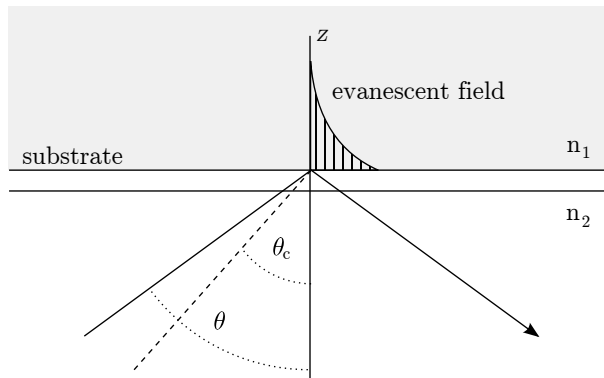

Fig. 6: Optical geometry of an objective type TIRF setup. The substrate is assumed to match the refractive index n_2.

2.2.2. Instrumentation

The optical microscope (*IX-71*, Olympus, Center Valley, PA, USA [30]) is equipped with a 60× oil immersion objective lens (*Plan Apo N*, Olympus, NA = 1.45,

$f = 0.13$–$0.15\,\mathrm{mm}$), a fluorescence filter-set and a TIRF unit. Fig. 7 shows the components and the light paths within the instrument. The AFM scanning stage is firmly attached to the microscope on top of its own movable stage, replacing the standard sample holder. The sample can be illuminated from above by a white light source and simultaneously from below by the excitation laser through a circular hole (ø $= 18\,\mathrm{mm}$) in the centre of the stage. The laser (*543-BS-A02*, CVI Melles Griot, Carlsbad, CA, USA) is an argon-ion gas laser, operating at a wavelength of $488\,\mathrm{nm}$. Its maximum continuous output power is $200\,\mathrm{mW}$; the laser can be adjusted to 50–100 % of that power. The device is installed outside the acoustic enclosure to avoid overheating and the incoupling of noise from the cooling fans running during laser operation. Its beam is conducted to the input port of the TIRF unit by a single-mode fibre optic cable (transmission $\approx$10–15 %). The TIRF unit has a single screw for controlling the beam offset and thereby the incident angle θ at the point of exit at the sample, compare Fig. 6. Usually, the smallest offset still resulting in total internal reflection is chosen, corresponding to $\theta = \theta_c$. From the TIRF unit, the beam passes through the aperture, controlling the size of the illuminated area, and is reflected at the dichroic mirror (*Z488 RDC*, Chroma, Rockingham, VT, USA). At the point of exit, the beam is totally internally reflected and only the evanescent wave is used to excite the fluorophores. To optimize the SNR, the aperture is closed until only an area with a diameter of 30–40 μm is illuminated.

The white background light, in contrast, is produced by a dimmable light source (*Fiber-lite MI-150R*, Dolan-Jenner Industries, Boxborough, MA, USA) and conducted into the acoustic enclosure by a fibre-optic light guide. It reaches the sample through the optical system within the AFM head, using the same light path as the the top-view camera.

The light emitted by the sample pervades the substrate and immersion oil (*Type B*; $n = 1.51$, Cargille, Cedar Grove, NJ, USA) before being collected by the objective lens, then passes through the dichroic mirror, separating out the laser excitation light, and through the bandpass emission filter (*XF3304*, Omega, Brattleboro, VT, USA) eliminating scattered light from the AFM tip positioning system. The filter is only transmittant in a narrow window of (605 ± 20) nm, thereby eliminating most other sources of optical noise as well. The remaining fluorescent light is then directed to the camera's output port by means of a set of movable mirrors. Note that both the excitation and fluorescent light has to pass through the sample substrate. In between the microscope's output port and the main camera an additional $1 - 4\times$ magnification lens is installed. It can be used to quickly change the magnification
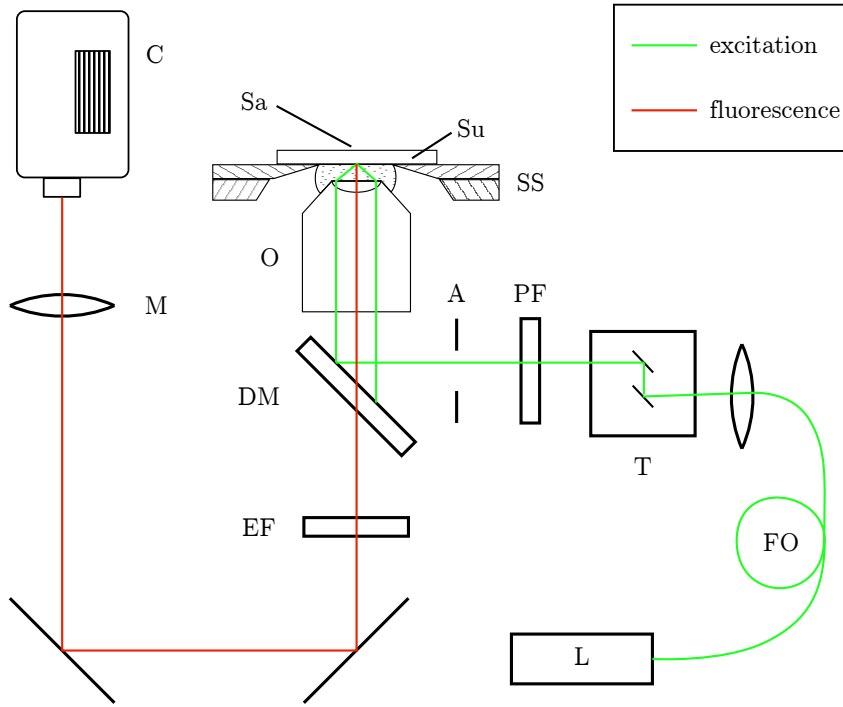
Fig. 7: Drawing of the optical components used in the setup. O: 60× immersion objective, C: EMCCD camera, L: Ar-Laser, FO: fibre optic cable, DM: dichroic mirror, EF: emission bandpass filter, PF: polarization filter (optional), A: aperture, M: 4× external magnification, T: TIRF unit, SS: Scanning stages, Su: substrate, Sa: sample.

when switching from quick overview images to sensitive and high resolution data acquisition. The final image size is approximately $128 \times 128\,\mu m^2$, divided by the additional external magnification. Usually this magnification is locked at the highest magnification available, i. e. 4× during the measurements, resulting in $32 \times 32\,\mu m^2$ optical images.

The images are captured using an electron multiplying charge coupled device or EMCCD (*Image-EM C9100-13*, Hamamatsu, Hamamatsu City, Japan). The camera can capture greyscale images, $512 \times 512\,px^2$ in size, at a maximum frame rate of $32\,Hz$. It has an analog gain of 5 and a electron multiplier gain of up to 1200, combined with a low readout noise of 1–20 electrons / readout, depending on the gain settings[28]. For the fluorescence emission of the quantum dots used (605 nm), the quantum efficiency of the CCD is >90 %. During operation, the CCD chip is cooled to −80°C by a Peltier element, practically eliminating thermal noise [28]; the excess heat is conducted out of the camera by a external water cooling system (*F25-ED*, Julabo Labortechnik, Seelbach, Germany).

The camera is connected to a computer using a frame grabber card. It is control-led by the imaging software *HCImage* (Hamamatsu). Apart from triggering the capture process, the software is used to adjust the CCD temperature and various imaging parameters. Images are saved as 8-bit greyscale TIFF files. The camera can capture 16-bit images as well, but since the Shot noise scales with the number of photons captured (but not with the value assigned to that number by the ADC, see Eq. (5)) the quality of the images would not increase articulately and has to be traded off against the higher noise and the computationally more intensive image processing. Multiple images of the same area are captured under identical condi-tions for statistical analysis, compare section 2.2.3. Even though the software does not report the photon count rates explicitly, they can be calculated from the image using the following equation

$$N_{ph} = (\zeta - \zeta_0) \cdot \frac{\text{GCF}}{\Gamma_{EM} \cdot \Gamma_A} \, , \tag{7}$$

where ζ_O is the camera's offset (dark current), GCF the gain conversion factor and Γ_{EM} and Γ_A the EM- and analog gain, respectively [31]. The EM gain deceases during the lifetime of the sensor and its exact determination would require a costly recalibration of the camera. Instead, the EM gain is estimated to be $(80 \pm 20)\,\%$ that of a new camera, based on the experience of Hamamatsu.

Since the AFM tip cannot be moved in the x- and y-direction, the whole optical stage has to be positioned correctly relative to the objective lens before the imaging process can begin. This is achieved by turning on both the laser and the white background light and moving the stage until the laser spot comes close to the AFM tip as seen from the auxiliary top view CCD camera. Then the AFM tip, which has to be very close to the surface or, optimally, already false engaged is usually already positioned within the field of view of the main camera. The external mag-nification can then successively be increased. When the tip is finally positioned in the centre of the image at full magnification, it roughly has a $16\,\mu$m margin to each side, guaranteeing that the smaller AFM image will be somewhere inside the area imaged optically. This is not to be confused with the sample alignment, which is described in section 4.2.1. The sample, mounted on the scanning stage, can be moved independently in between the tip and the objective. If the sample is prone to photobleaching, for example, the scanning stage can be moved at any time to an area of the sample that was not yet exposed to the laser light, without disturbing the alignment of the AFM with the optical axis.

In principle, live images can be captured during the scanning process, but this requires the laser and camera (incl. the water cooling) to be active, inducing large amounts of noise in the AFM image. Therefore, optical images are usually taken before and after the scanning process, with the tip hovering above the surface.

2.2.3. Image analysis

The image quality is dependent on three major factors: The SNR, the signal shape and distribution of the peaks and the total number of photons collected. The latter can be derived from the greyscale value of each pixel using Eq. (7). The photons of all pixels within two standard deviations of each peak's centre are summed up to give the total photons per peak. Concerning the density of the fluorophores, it is desirable to have many of them in the image, but as few overlapping signals as possible. Depending on the substrate used (see section 3.2), the signal shape complies more or less with the assumed 2D-Gaussian. The actual effect of the shape on the fitting precision can be measured by comparing multiple images, see below.

For determination of the SNR, the mean background of the image is calculated by selecting an area by hand that is sufficiently large and does not contain any signals. The mean value of all pixels in that area is taken to be the mean background b'. The conversion to photon count rates ($b' \to b$) is performed according to Eq. (7). The SNR can then be computed according to Eq. (6), using the mean height $\bar{\zeta}_{max}$ of the peaks to be fitted.

2.3. Superlocalization

2.3.1. Idea

Superlocalization (a. k. a. FIONA) "reverses" the effect of diffraction by fitting the known PSF of a single emitter to its diffraction limited image, thereby revealing its position $\vec{o} = (\xi, \upsilon)$ with high accuracy. The idea that the position of a single emitter can be determined with high accuracy — despite the diffraction — has already been formulated by Heisenberg in 1930, see p. 17 in [32]. In 1986, the theory was elaborated in detail by Bobroff [14] and in 2003 applied by Yildiz et al. [12] to single fluorophores in a biological context. The maximum accuracy that can be achieved by this technique does not only depend on the instrument's resolution, but rather on the image's quality, described in terms of its SNR, pixel size, etc. Typically

this technique can be used to obtain positional information that is 1–3 orders of magnitude more precise than the optical image's resolution [33].

2.3.2. Implementation

A 2D-Gaussian function used for the fitting. It is easier to handle mathematically than the Airy function, but provides excellent results, even if the signal is not perfectly Gaussian shaped [34]. For each spot to be fitted, a square area (ROI), with the peak in its centre is designated accordingly. The ROI is chosen to be as large as possible (2–3 times the diameter of the peak as perceived by the eye), but without including any signal from neighbouring peaks. For each of the peaks, the analysis software will try to fit the function g of Eq. (4) to the brightness distribution $\zeta(i, j)$ within that region by minimising

$$\sum_{i,j} \left(\zeta(i, j) - g(i, j) \right)^2, \tag{8}$$

where the sum runs over all pixels (i, j) of that ROI. Fig. 8 shows an example of a successful fit.
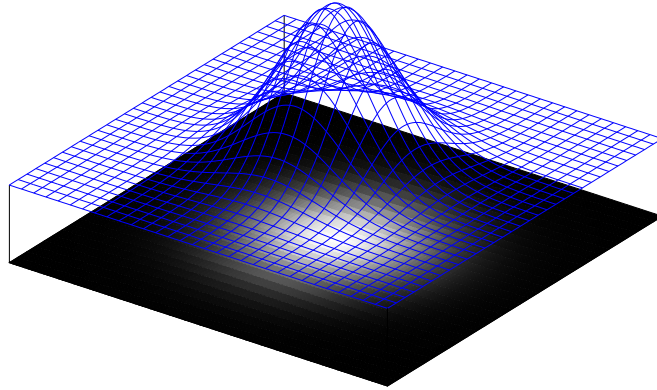

Fig. 8: Illustration of the fitting process. The fluorescence signal is shown at the bottom, the fitted Gaussian as a grid on top.

2.3.3. Error calculation

A formula to calculate the expected superlocalization accuracy of a single image has been derived by Thompson et al. [15]:

$$s_F = \sqrt{\frac{s_g^2}{N} + \frac{a^2}{12\,N} + \frac{8\pi s_g^4 b^2}{a^2 N^2}}\,. \tag{9}$$

The symbols denote the width of the PSF s_g, the pixel size of the capture device a, the total number of photons in a peak N and the background b. The three additive terms correspond to the photon shot noise, the rasterization error and the background noise, respectively. This formula is practical, since it can be evaluated without requiring further measurements. Additionally, it provides a physical understanding of the errors. However, it assumes that the signal shape perfectly equals a Gaussian and it relies on the absolute photon count rates, which cannot be obtained very precisely, see Eq. (7).

Therefore, the precision of the fit is evaluated stochastically by applying the fitting algorithm to multiple images taken of the same area, as suggested by Rust et al. [35]. Even if neither the position of the fluorophores nor the imaging conditions have changed (as is assumed), the images will not perfectly look alike. As a result, slightly different sets of coordinates will be output for each image j and the deviation of these independently fitted positions $\vec{o_i} = (\xi_i, \upsilon_i)$ can be used to determine the precision of the fits for that set of images:

$$s_O = N_R^{-1} \cdot \sum_i^{N_R} \left(\frac{\sum_j^{N_I} \sqrt{\left(\xi_{ij} - \bar{\xi}_i\right)^2 + \left(\upsilon_{ij} - \bar{\upsilon}_i\right)^2}}{\sqrt{N_I - 1}} \right) . \qquad (10)$$

Here i runs over all N_R selected regions, each containing one peak, while j enumerates the N_I images. Of course, the sum over i can be omitted to calculate the precision of a single peak, compare Fig. 9. If the fitting precision of a single peak is considerably lower than the average, it is excluded from further analysis, according to the criterion of Chauvenet, see p. 57 in [36]. In general, this "internal" method of determining the uncertainty is more precise and to be preferred over the "external" method, i.e. using Eq. (9), since it is based on experimental data and does not require any assumptions (e.g. about the signal shapes), compare p. 37 in [36].

Before the combination of the two techniques AFM and fluorescence superlocalization is described in chapter 4, the samples and substrates used for the experiments will be briefly discussed.
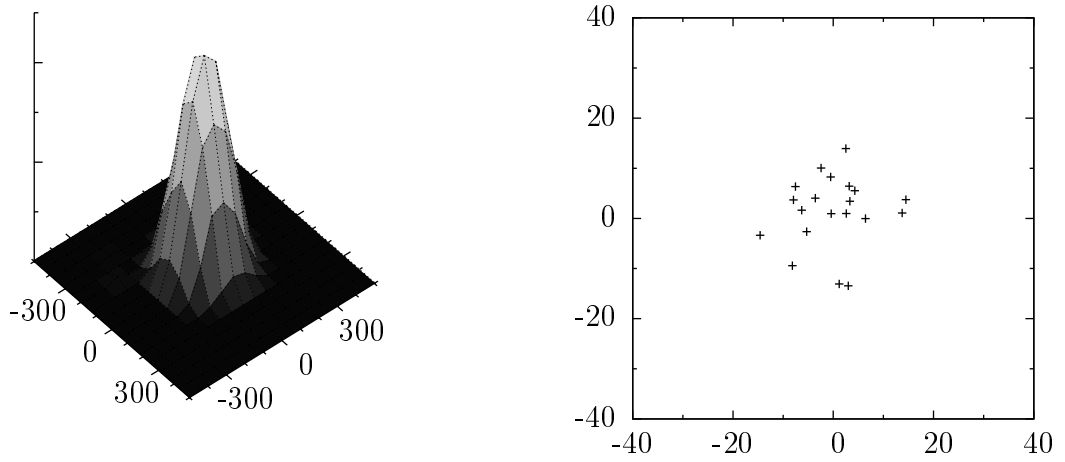
Fig. 9: 3D representation of a fluorescence peak (left) and the fitted position of its centre obtained from $N_I = 20$ single images of the same area (right). Units = nm.

3. Substrate & Sample Optimization

A major challenge of this work was to optimize the sample preparation for both optical and topographical imaging. For AFM, the most important substrate properties are mechanical stability, cleanness and low roughness, while for single molecule fluorescence imaging low absorbance, auto-fluorescence and signal distortion are needed. While these the requirements are not mutually exclusive, it is hard to find a material that is suitable for both. In comparison, the choice of fluorophore was straightforward: quantum dots are almost ideal candidates for the technique.

3.1. Quantum dots

Semiconductor nanocrystal quantum dots (QDs) are suited fluorophores for this work, since they can easily be identified in both AFM and optical images. Their advantages, compared to other fluorescent dyes, include the high absorption, photostability and Stokes shift, compare p. 675ff in [5]. By varying the size and material of the QDs, their optical properties can be tuned almost arbitrarily. The quantum dots used for this work *(Qdot 605*, Invitrogen, Carlsbad, CA, USA) are CdSe nanocrystals, coated with a ZnS layer and a polymer that is not explicitly specified (see [37] for a review of typical materials). Secondary antibodies (goat anti-mouse) are attached to the core, that will effectively bind to a broad range of commercially available monoclonal mouse antibodies. The total size of a coated QD is 10–15 nm [38]. Because of their height and rigidity, they can be easily told apart from biological macromolecules directly in the AFM images. Their emission spectrum is rather narrow and has its maximum at 605 nm, see Fig. 10. The optical system has been optimized for this wavelength, so that it can be clearly separated from both the excitation laser and the AFM positioning SLD.

While quantum dots are not much affected by photobleaching, they show a "blinking" behaviour rather similar to single organic fluorophores [40]. The emission of
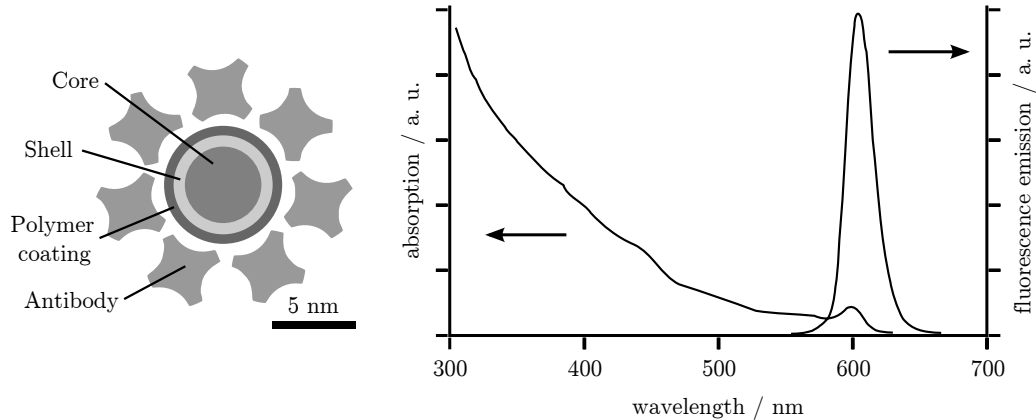
Fig. 10: Structure and spectra of the "Qdot 605", adapted from [39].

this type of quantum dot has been studied by Brokmann et al. [41], with particular emphasis on the emission properties when close to dielectric interfaces, as in the present experiment. For a more general discussion of their optical properties, see p. 309ff in [23] and p. 675ff in [5].

The quantum dots are stored at a concentration of $1\,\mu$M at 4°C and diluted to a concentration of 50–100 pM right before the deposition in the according buffer (see Appendix A.2). The concentration has to be optimized for each type of substrate in order to have as many molecules in the field of view as possible, without putting up with too many overlapping optical signals.

Typically, the QDs are diluted in the deposition buffer to a concentration of 50–500 pM and 15–20 μl of the suspension are drop casted onto a clean substrate. After 10–20 s the remaining buffer is rinsed away with ultra pure water and the sample is blown dry using pure nitrogen. The so prepared samples are then immediately mounted in the microscope or stored in the dark for no longer than a few hours.

3.2. Substrates

The substrates evaluated include glass, brown mica, quartz, MgO, and mica glued on glass using immersion oil. Mica [42] is a type of sheet silicate mineral, that can be easily split along its crystallographic (0 0 1) structural plane, resulting in an almost perfectly flat and clean surface. It is therefore often used as a substrate for single molecule AFM imaging, see p. 187ff in [19], for example. Mica was ordered as $75 \times 25 \times 0.15\,\text{mm}^3$ slides, grade V-5 (Structure Probe, West Chester, PA, USA) and then cut into smaller pieces (roughly $10 \times 20\,\text{mm}^2$) using a scalpel. The mica was cleaved several times by sticking adhesive tape to its top surface. When removing
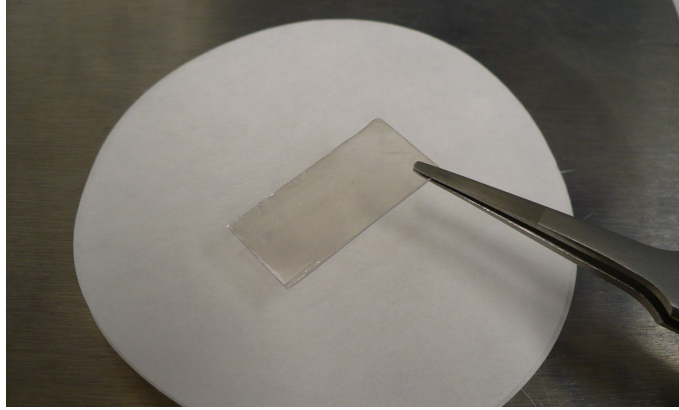
Fig. 11: A freshly cleaved sheet of mica.

the tape, some sheets of mica will lift off with it, ideally resulting in an atomically flat surface.

For the experiments on glass, *Goldseal Cover Glass 260300* (Corning, New York, USA), available as $22 \times 22 \times 0.1\,\mathrm{mm}^3$ slides, is used, since it is considerably smoother than any other glass substrate known to the author, compare [43] or [44], for example. Quartz and MgO substrates were ordered as $10 \times 10 \times 0.15\,\mathrm{mm}^3$ slides (Surface.net, Rheine, Germany). As these are too small to be directly mounted on the AFM stage (diameter of the hole: $18\,\mathrm{mm}$), they are taped down on a thin metal plate with a $9.0\,\mathrm{mm}$ hole, which can in turn be fixed magnetically to the stage.

Except for the mica substrates, the surfaces are cleaned and chemically polished by immersing them into different chemicals and sonicating them, as described in [44]. The protocol that worked best consists of one hour sonification in $3\,\mathrm{M}$ KOH, thorough rinsing with ultra pure water, followed by one hour sonification in $100\,\%$ Ethanol (p. a.). The mica-glass-stack samples were prepared by gluing a freshly stripped piece of mica to a cover-slip glass using approx. $1\,\mu\mathrm{l}$ of immersion oil.

3.3. Evaluation

Initially, the different substrates were qualitatively tested for their roughness, cleanness and optical properties, see Table 1. Without further investigations, quartz and MgO were ruled out, because the substrates had to be cleaned and reused, which makes it difficult to achieve an acceptable cleanness. The mica-on-glass type of samples was dropped because of its height (working distance of the objective is only $150\,\mu\mathrm{m}$) and bad optical properties. Glass, being the best optical substrate, and mica, the best substrate for AFM, were then investigated in more detail.

substrate	roughness	cleanness	optical quality
Glass	−	o	+
Mica	+	+	o
Mica on glass	+	+	−
Quartz	o	−	o
MgO	o	−	o

Table 1.: Qualitative classification of different substrates according to their surface and optical properties (+ good, o tolerable, − problematic).

Optical properties. The most prominent difference, visible to the naked eye, is mica's brown colour opposed to the clear glass. The colour is determined by small amounts of Cr, Fe or other impurities present in the crystal. This indicates a higher absorbance and indeed, the signal intensity is reduced by approximately 10–20 %, compared to an equally thick glass substrate (data not shown). While this can be compensated by longer exposure times or higher gains, the best way to deal with it is to use thinner micas. Furthermore, the signal shapes are deformed when imaging on mica, see Fig. 12. These altered shapes likely arise from the mica's birefringence, along with the fact that its refractive indexes ($n_\alpha \cong 1.56$, $n_\beta \cong 1.59$, $n_\gamma \cong 1.60$) [42] don't match the one of the immersion oil ($n = 1.51$). This mismatch is enough to make proper focusing impossible. No single focal point exists anymore for light entering the objective at different angles, compare p. 778f in [5]. For micas that aren't too thick, the patterns resemble those observed by Brokmann et al. [41] imaged slightly out of focus.

However, both the perceived extent of the distortions and their influence on the superlocalization precision decrease along with the thickness of the mica sheet. The dependence of the precision on the mica's thickness was quantitatively examined, too, see Fig. 13. Although no linear relationship was found, a trend towards better fitting precision exists for thinner micas. Thin sheets can therefore be considered suitable optical substrates. Unfortunately, the substrate can't be made arbitrarily thin, since very thin sheets of mica ($< 20\,\mu$m) are too elastic, thus not providing enough stability for AFM imaging.

For reference purposes, Table 2 lists the typical properties of single fluorescent signals on glass and mica.

Surface properties. The adsorbance properties of both substrates are roughly comparable. The concentration of quantum dots in suspension resulting in a optimum coverage is 30–60 % lower on glass, typically 70–100 pM, compared to 100–
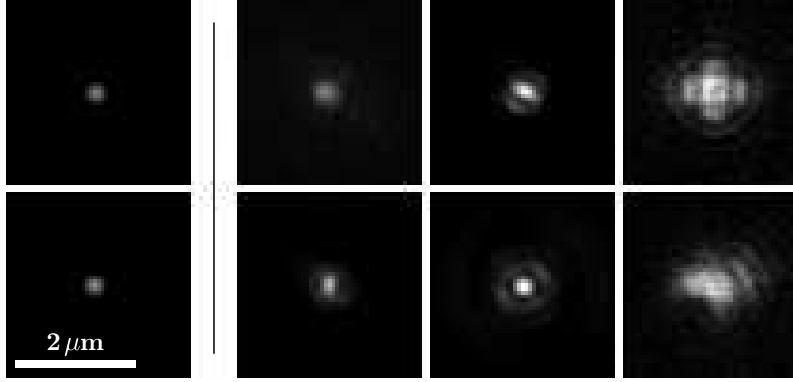
Fig. 12: Signal shape on different substrates. Left: glass, right: mica sheets with varying thickness. Lateral dimensions to scale, brightness normalized.
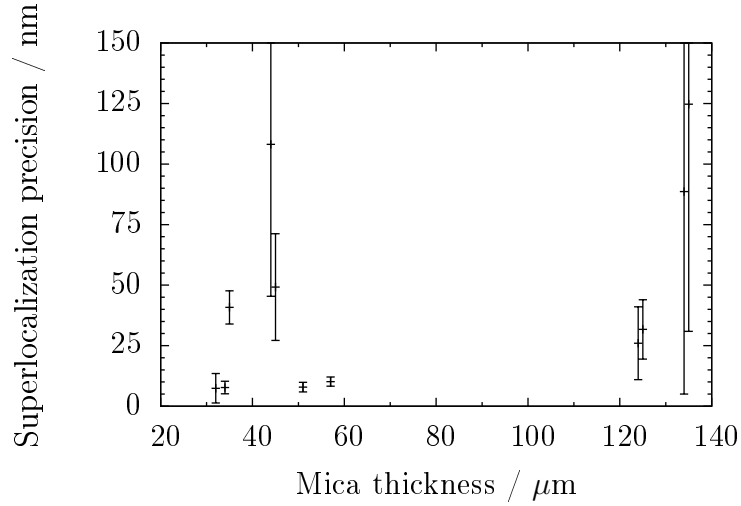

Fig. 13: Effect of a mica sheet's thickness on the superlocalization precision. The precision is obtained according to Eq. 22 by fitting 5–10 peaks in 15–20 single images for each data point, compare Fig. 23.

substrate	width / nm	area / μm^2	total photons	maximum / photons
Glass	380 ± 20	0.12 ± 0.02	1700 ± 500	350 ± 200
Mica	780 ± 350	0.57 ± 0.42	1600 ± 800	200 ± 150

Table 2.: Properties of a typical fluorescent signal (single peak). The photon counts include 0.2–5 % background, depending on the exposure and gain settings. These are chosen to exploit the full scale of the image, while trying to keep the background as low as possible.

substrate	roughness (rms) pm	highest particles nm	abundance of "dirt" particles / μm^2
Glass	280 ± 100	1–5	0.2–1
Mica	80 ± 15	0.2–0.4	N. A.

Table 3.: Roughness and cleanness of glass and mica substrates before sample deposition. For comparison: under the given imaging conditions, DNA appears ~ 0.5 nm high.

300 pM on mica. The remaining surface properties measured agree with the values published for comparable substrates (e. g. glass: [21], mica: [45]) and are summarized in Table 3.

Conclusion. Both substrates are possible candidates for this technique. However, the roughness and cleanness of glass could not be ameliorated, while the optical properties of mica improve with decreasing substrate thickness. Therefore, thin slices (20–50 μm) of the mica are considered to be most suitable for biological imaging, cf. Table 2.

4. Registration

In the previous chapters, the acquisition of the experimental data by AFM and fluorescence microscopy have been described. The combination of these techniques has been used by other research groups [44, 46, 47]. However, it is specific to this method that additional positional information is gained from the fluorescent images (rather than spectroscopic data). Using superlocalization and the image registration method described in the following paragraphs, single labelled proteins can thereby be identified, even in the presence of many identical or similar macromolecules.

4.1. Transformation

In order to relate the information from the two different sources AFM and fluorescence, the corresponding images have to be aligned. In the end, information that originates from the same point in space should be displayed at the same point in the composite image. Mathematically speaking, this is done by a transformation from one image's coordinate system into the other's. One of the source images, called template or projection image will be transformed to match the other one, called reference image. For this method, the AFM image is used as the reference. The determination of the optimal transformation for registration depends on the types of variations between the images [48]. Here, an affine transformation (see p. 195ff in [25]) is used to align the projection image. This type of transformation maps each point $\vec{o} = (\xi_i, \upsilon_i)$ onto $\vec{o}^\star = (\xi_i^\star, \upsilon_i^\star)$ as follows

$$
\begin{pmatrix} \xi_i^\star \\ \upsilon_i^\star \end{pmatrix} = \begin{pmatrix} m_{11} & m_{12} \\ m_{21} & m_{22} \end{pmatrix} \begin{pmatrix} \xi_i \\ \upsilon_i \end{pmatrix} + \begin{pmatrix} t_1 \\ t_2 \end{pmatrix}
$$

$$
\vec{o}^\star = \hat{m}\,\vec{o} + \vec{t}.
$$

(11)

The six parameters in $\hat{m}$ and $\vec{t}$ have to be determined by the registration algorithm. Even though the values have to be computed for each particular image, some general

remarks about the form of $\hat{m}$ and $\vec{t}$ can be made, taking into account the specific setting of this experiment. In this particular situation, the transformation matrix $\hat{m}$ is composed of a scaling and a rotation only. The scaling factor is given by the proportion of the pixel resolutions of the AFM image r_A and the optical image r_O, respectively. Because the camera is roughly aligned with the AFM, the angle of rotation between the two images, β, is almost zero. Therefore, small-angle approximation may be used for the rotational part, resulting in the following assessment

$$\hat{m} = \begin{pmatrix} r_A/r_O & 0 \\ 0 & r_A/r_O \end{pmatrix} \cdot \begin{pmatrix} \cos\beta & -\sin\beta \\ \sin\beta & \cos\beta \end{pmatrix} \cong \frac{r_A}{r_O} \begin{pmatrix} 1 & -\beta \\ \beta & 1 \end{pmatrix}. \qquad (12)$$

It would be possible to define a transformation that corrects zoom and rotation only, i.e. $m_{11} \equiv m_{22}$, $m_{21} \equiv -m_{12}$, containing two parameters less. However, experimentally, the full affine transformation showed slightly better performance, probably because it can account for the small remaining thermal drift (despite the stabilized environment) that skews the AFM image slightly (data not shown). Nevertheless, the deviations from the form of Eq. (12) are typically $\ll 1\,\%$.

The translation $\vec{t}$ is equal to the distance of the rotational centre in the AFM image $(\bar{x}, \bar{y})$ and in the optical image $(\bar{\xi}, \bar{v})$, brought to the same scale:

$$\vec{t} \cong \begin{pmatrix} \bar{x} \\ \bar{y} \end{pmatrix} - \frac{r_A}{r_O} \begin{pmatrix} \bar{\xi} \\ \bar{v} \end{pmatrix}. \qquad (13)$$

These centres are equal to the mean x and y coordinates of the fiducial markers, see section 4.1.3. A formal description of this and other transformations can be found in [49] on p. 27f, a more practical discussion with focus on image processing in [50], p. 29ff.

4.1.1. Landmark-based registration

Given the transformation to apply, image registration is an optimization problem, minimizing the "distance" between two images by modifying the transformation. This is a common problem, e.g. in the computer sciences, and has been intensively studied and solved in different contexts [48]. Depending on the problem, diverse algorithms exist, including principle axis-based registration, optimal linear registration and a whole family of non-parametric image registration methods, see p. 1ff in [49]. To determine the "distance" between two images, however, most image registration algorithms use some figure of merit based on the similarity of the images [48].

For these methods to function, both images have to contain a significant amount of mutual information, which is routinely not the case for the combination of AFM and fluorescence. There are various reasons for this: Firstly, not all features visible in the AFM image are optically active, and even if they are, their representations in the two images don't look alike. Secondly, when imaging single molecules, most of the area of a typical image is empty (except for noise) and hence can't contribute to the calculation. Taking that into account, the choice of registration methods basically boils down to one technique: landmark-based registration.

The method of landmark-based registration is probably the most basic image registration. A number of N_F corresponding positions are selected as so-called fiducial markers in both images, cf. Fig. 14. The positions of three fiducial markers (corresponding to six coordinate pairs) are needed as input to determine the six parameters of the transformation. Additional pairs over-determine the transformation and can be used to analyze its accuracy. For this type of registration, the "image distance" is given by the mean real distance $\bar{d}$ of corresponding markers after the transformation has been applied. Given the AFM coordinates $\vec{a}_i = (x_i, y_i)$ and the transformed fluorescence coordinates $\vec{o}_i^\star = (\xi_i^\star, v_i^\star)$, $\bar{d}$ can be computed as

$$\bar{d} = \sum_{i}^{N_F} \left(\vec{a}_i - \vec{o}_i^\star \right) , \tag{14}$$

where i enumerates the N_F fiducial markers chosen. The algorithm then tries to minimize $\bar{d}$ by optimizing the parameters for the transformation in Eq. (11). The complexity of the registration task is not reduced by this technique, though, but rather transferred to the task of finding appropriate fiducial markers, compare p. 36–41 in [51]. Depending on the choice of markers, landmark-based registrations will not always produce a meaningful result, see p. 44 in [49]. Even though these limitations greatly complicate the automation of the registration, this approach is leading to the desired results, since either the set of valid results can be regularized, cf. p. 4ff in [49], or — as done in this work — the choice of fiducial markers and the result of the transformation can be monitored by the user and, if need be, corrections can be made on a case-by-case basis.

4.1.2. Output format

When the transformation has been computed, the whole optical image can be aligned to the AFM image and then be displayed on top of the topographical data, e. g. as a
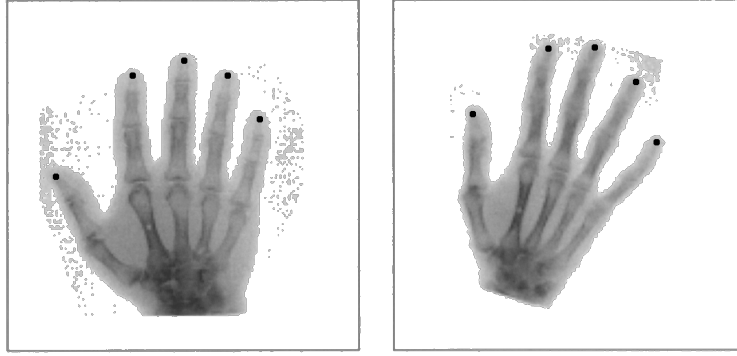
Fig. 14: Illustration of a landmark-based registration. Corresponding positions are selected as fiducial markers in both images (dots), providing information on how to transform the template image. From [52].

colour overlay. However, looking at Fig. 19, which is produced this way, it becomes immediately obvious that single proteins can't be identified from the superimposed fluorescence signal. Because of its diffraction limited size, large areas in the AFM image are covered by a single fluorescent spot. Therefore, rather than displaying the aligned fluorescence image, a new image is created with the dimensions of the AFM scan, containing the positional information from the superlocalization of the optical signals, similar to the PALM technique [11]. At each fitted position $(\xi_i^\star, \upsilon_i^\star)$, a 2D-Gaussian is placed with a width of $s_{o,i}$, corresponding to the uncertainty in the spot's position. This positional information can then again be displayed as a colour overlay, which is a clear and intuitive way of presenting the information, see Figs. 19, 20, 33 on pages 42, 43, 56.

4.1.3. Error analysis

The error of the transformation's parameters can be numerically determined and output by *Mathematica*'s built-in functions, but the following discussion leads to a more "physical" understanding of the uncertainties.

Beforehand, the use of the two terms accuracy and precision in context of the landmark-based registration will be briefly discussed, q.v. p. 2f in [36]. In general, *accuracy* refers to the proximity of a measured quantity to the real value, while the term *precision* indicates how reliably a result has been determined. While the first arises from systematic errors, the latter is caused by random statistical fluctuations and usually identified with the standard deviation of a number of measurements. For determining the accuracy experimentally, obviously the true value has to be known and for obtaining the precision, a number of comparable data sets must exist. If

a value is measured accurately, but imprecisely many times, its true value can be obtained with high fidelity by means of statistical analysis. The converse argument is not true, therefore experiments should typically be designed to be limited by the precision, i. e. the statistical error, as illustrated in Fig 15, compare also p. 2, 38f in [36].
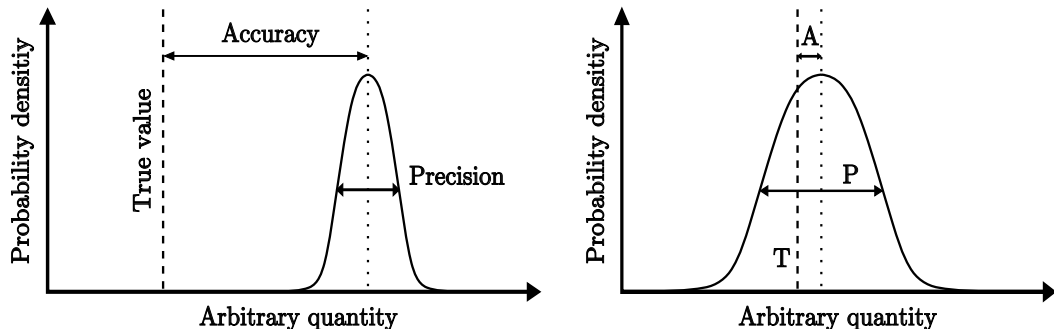

Fig. 15: Illustration of the terms accuracy and precision. A quantity is measured and the probability — or abundance — of each result is recorded and compared to the known true value. In the two examples, the left measurement is rather precise but inaccurate, while the right one is more accurate but imprecise.

Cheezum et al. [26] have shown that the positional information obtained by super-localization is not biased, at least for well-formed signals. Its uncertainty is therefore of purely statistical nature, cf. section 2.3. The position of each transformed fiducial marker can be compared to the known position of the fluorophore in the AFM and is therefore of the type of an accuracy. For evaluating the significance of a result, both types of errors have to be considered, of course. Following this short excursion, the contributions to the error of the registration shall now be discussed.

The mean error of the registration s_R, i. e. the error of the positions of the fluorescent markers transformed to match the AFM image $\vec{o}^\star = (\xi_i^\star, \upsilon_i^\star)$, can be computed by inserting their original positions in the optical image $\vec{o} = (\xi_i, \upsilon_i)$ into the transformation given by Eq. (11) and applying the laws of error propagation:

$$s_R^2 = \left(\frac{\delta \vec{o}^\star}{\delta \hat{m}}\right)^2 s_m^2 + \left(\frac{\delta \vec{o}^\star}{\delta \vec{o}}\right)^2 s_O^2 + \left(\frac{\delta \vec{o}^\star}{\delta \vec{t}}\right)^2 s_t^2 . \tag{15}$$

Here s_m and s_t are the uncertainties of $\hat{m}$ and $\vec{t}$, respectively and s_O is the mean of the errors of all individually fitted fluorescent signals $\bar{s}_{o,i}$. The partial derivations with respect to $\vec{o}$ and $\vec{t}$ can be easily interpreted physically as the norm of the partial

34

derivatives of their x and y elements, i.e.

$$\left(\frac{\delta\vec{o}^{\star}}{\delta\vec{v}}\right)^2 s_t^2 := \left(\frac{\delta\vec{o}^{\star}}{\delta v_1}\right)^2 s_{v_1}^2 + \left(\frac{\delta\vec{o}^{\star}}{\delta v_2}\right)^2 s_{v_2}^2 \,, \tag{16}$$

where $\vec{v} = \vec{t}$ or $\vec{o}$, respectively. However, the derivation with respect to $\hat{m}$ can't be simplified in a straightforward manner. Instead of interpreting the derivative, the influence of errors in $\hat{m}$ is analyzed, as illustrated by Fig. 16. The absolute error induced by inaccurate transformation parameters scales with the distance from the centre of the transformation, which is equal to the centre of mass of the fiducial markers. The mean positional uncertainty of the fiducial markers is roughly equal to $\bar{d}$, the mean distance of matching pairs of transformed fiducial markers. If the markers are spread evenly on a concentric circle, all spots within this circle have a smaller error, while those outside have a larger than $\bar{d}$, compare Fig. 16. If the circle was enclosing 68 % of the image area (and thus a corresponding fraction of all signals), $\bar{d}$ would be representative for all positions in the image. Even if the markers are not exactly placed on a circle, this approximation is still valid, as long as the markers are spread more or less evenly across the image. Therefore, the first summand in Eq. (15) can be replaced by $\bar{d}^2$. Although this consideration does not take into account that points near the centre are placed more accurately, it provides a simple measure of the mean value of s_m.

Applying the definition in Eq. (16) to Eq. (11), the corresponding derivatives can be evaluated to $\delta\vec{o}^{\star}/\delta\vec{t} = 1$ and $\delta\vec{o}^{\star}/\delta\vec{o} = \hat{m}$. Thus Eq. (15) can be simplified to

$$s_R^2 = \bar{d}^2 + s_t^2 + \hat{m}^2\, s_O^2 \,. \tag{17}$$

Considering that $\vec{t}$ is given by Eq. (13), i.e. equal to the difference between the centre of mass of the fiducial markers in the AFM image $(\bar{x}, \bar{y})$ and in the optical image $(\bar{\xi}, \bar{v})$, brought to the same scale, s_t can be computed as follows

$$s_t^2 = s_A^2 + \left(\frac{r_A}{r_O}\right)^2 s_O^2 \,. \tag{18}$$

Here, s_A and s_O are the mean errors of the AFM and optical positions and r_A and r_O the corresponding pixel resolutions of the images. The error of the AFM positions s_A is considered to be half the pixel size, as described in section 2.1.3. The error of the superlocalized positions of the fluorescent spots s_O is given by Eq. (10) in section 2.3.
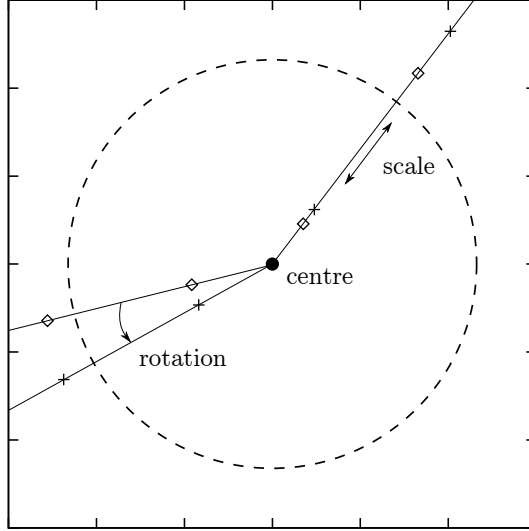
Fig. 16: Effect of scaling and rotation errors in an affine transformation (diamonds: correct positions, crosses: wrongly transformed positions). Both errors scale linearly with the distance to the centre of the transformation. All points inside a concentric circle of any diameter have smaller errors than those outside the circle.

Finally, the term $\hat{m}\, s_O$ needs to be discussed. Looking at Eq. (12) again, one can deduce that the rotation does not affect the magnitude of s_O at all — the scaling however does. Therefore $\hat{m}$ can be reduced to a scalar: $\hat{m} \rightarrow m = r_A/r_O$, resulting in a final equation for the total error of the registration

$$s_R = \sqrt{\bar{d}^2 + s_A^2 + 2 \cdot \left(\frac{r_A}{r_0}\right)^2 s_O^2}\,. \tag{19}$$

This simplified equation for s_R is valid under the assumptions that the fiducial markers are spread evenly across the image and placed in a meaningful way, i.e. no false assignments of fiducial markers are made. Furthermore it neglects possible stage drifts or lens distortions and the dependence of the error on the distance from the centre. In exchange, s_R can be readily computed from the experimental data, independent of the placement of the fiducial markers.

Finally, for display purposes, $s_O \cdot r_A/r_O$ is taken out of the above equation, but instead the individual $s_{o,i}$ of each spot is displayed as the width of a Gaussian distribution in the overlay image, placed at the fluorophore's superlocalized position, as described in section 4.1.2.

4.2. Implementation

Basically, the process of registration consists of finding fiducial markers, determining their positions with high accuracy, calculating a transformation to align the images and displaying the result. All of these tasks require the handling of rather large amounts of data and extensive numerical calculations. For the implementation, *Mathematica* [53] was chosen as the programming language due to its high level implementation of optimization problems, e.g. `FindFit`, `Minimize`, etc., combined with the built-in image processing capabilities. The code used for this task is printed in Appendix A.3. All computations are performed using pixel coordinates and only the final results are converted to absolute values (nm) by multiplying them with the appropriate pixel resolution.

4.2.1. Raw alignment

The optical image is most often several times larger than the region scanned by the AFM. Before proceeding with the analysis, it is therefore necessary to "raw align" the images in order to identify the scanned region in the optical image. Reliable algorithms for finding spots in a single image exist [54, 55], but finding matching pairs in two images acquired independently is a more daunting task, that cannot be easily automated, cf. p. 45 in [49]. Even if the positions of all spots are known in both the AFM and the fluorescence image, but some fluorophores are optically inactive — a general problem in single molecule fluorescence — the search for a matching pattern is already a challenge. The number of possible combinations (permutations) that have to be tested scales like

$$N_i \cdot \frac{N_i!}{(N_i - N_a)!} \,, \tag{20}$$

where N_i is the total number of peaks and N_a the number of the optically active ones in a given image, cf. p. 766ff in [25]. Furthermore, no reliable algorithm is known to the author that performs well even if the number of markers is the same in both images, but the form of the peaks is not. Therefore both the selection of features to be fitted and the identification of matching pairs to be used as fiducial markers is done by hand.

One starts by identifying a larger region in the optical image as the one corresponding to the AFM scan by looking at images with the back light turned on, i.e. showing the shadow of the cantilever on top of the fluorescent peaks, see Fig. 17.
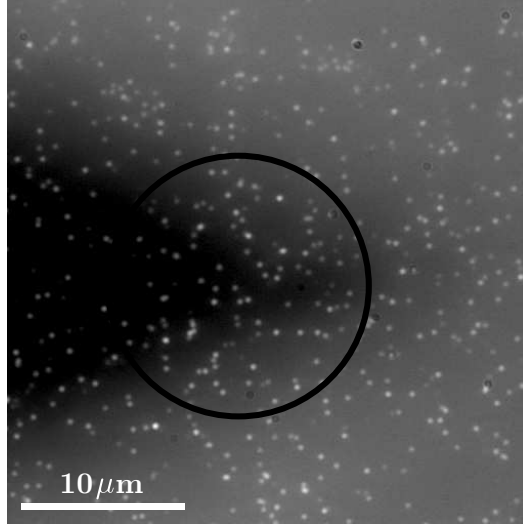
Fig. 17: Shadow of the cantilever, visible against the white background light. This kind of image can be used to identify the region scanned by the AFM. The encircled area is then searched for salient patterns.

Next, the whole area has to be scanned for patterns of fiducial markers that match those present in the topographical image. To alleviate the problem caused by blinking fluorophores, several images can be summed up to increase the number of active fluorophores in the template image. The advantage compared to increasing the integration time is that information on a time scale larger than that of the blinking can be collected while keeping the summed up exposure time short and thus the background noise low. The "pattern search" can then be performed on printouts of the images or using standard image manipulation software like *ImageJ* [56] or the *GIMP* [57].

Even though this "pattern search" is somewhat random and possibly biased, it is immediately evident if the correct region is found. If the raw alignment is correct, all remaining fluorescent signals can be visually related to a corresponding feature in the AFM image. The probability of a false assignment P_{fa} is extremely low, as shown by the following consideration. This probability is the same as the probability of Z randomly distributed fluorescence peaks (additional to the ones in the search pattern) to each fall within a certain area around a topographical feature of the image (p percent in size), given by

$$P_{fa} = \left(A \cdot \frac{p}{100} \right)^{Z} ,$$
(21)

where A is the number of topographical features in the AFM image that could
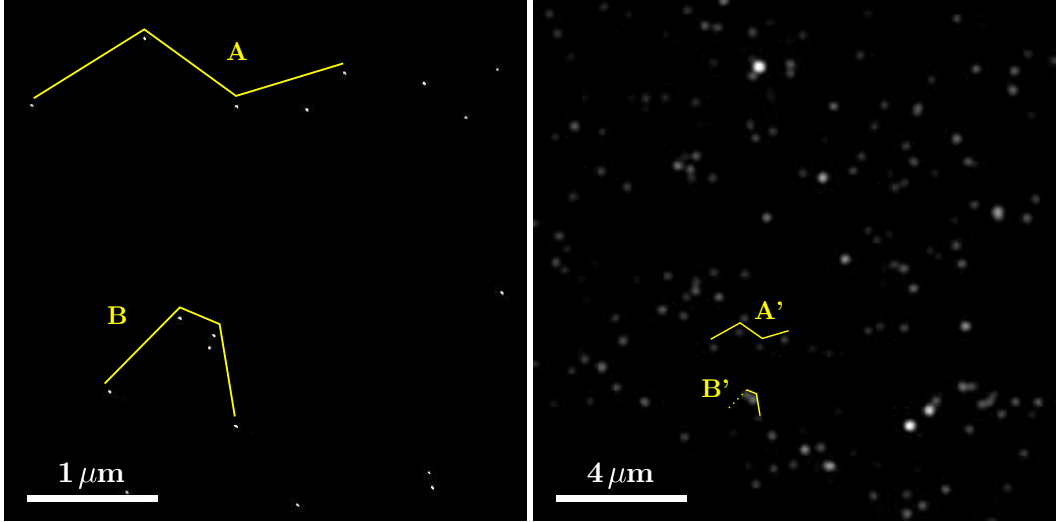
Fig. 18: Illustration of the "pattern search". AFM image (left) and optical image (right, detail only) of a quantum dot sample. The contrast is increased artificially to facilitate the recognition of patterns. **A**: matching pattern with well separated optical peaks. **B**: pattern with an optically inactive quantum dot and overlapping fluorescent signals.

correspond to a fluorophore. For a typical example, let $A = 3Z$ (assuming that ⅓ of the features visible in the AFM is labelled and can be fitted) and $p = 1\%$, corresponding to a $50 \times 50\,\text{px}^2$ box in a $512 \times 512\,\text{px}^2$ image. Then $P_{fa} = 2.8\%$, 0.33%, 0.06% for $Z = 1$, 2, 3 additional peaks, respectively, which is negligibly small.

Once this initial raw alignment has been achieved and a number of fiducial markers has been selected, the further analysis can be automated.

4.2.2. Calculation of the transformation

At first, the coordinates of the fluorophores have to be determined in both images, as described in sections 2.1.3 and 2.3, respectively. Of these coordinates, a set of N_F pairs of corresponding AFM $\vec{a}_i = (x_i, y_i)$ and optical $\vec{o}_i = (\xi_i, v_i)$ positions is chosen to be used as fiducial markers. Then the weighted sum

$$\Sigma_w = \sum_i^{N_F} \frac{\sqrt{(x_i - \xi_i^\star)^2 + (y_i - v_i^\star)^2}}{s_{o,i}^2} \,, \tag{22}$$

that runs over all pairs of fiducial markers N_F is numerically minimized. It implicitly contains the transformation parameters through $\xi^\star$ and $v^\star$, see Eq. (11). The

division by $s_{o,i}^2$, the variance of the single fitted fluorescence positions, ensures that coordinates which are known less precisely contribute less to the final result, compare [36], p. 56f. If the uncertainty in the AFM coordinates s_i isn't equal for all points, it has to be taken into account, too. The results of this minimization are the transformation matrix $\hat{m}$ and offset $\vec{t}$ in AFM image coordinates. To obtain the mean distance $\bar{d}$ between matching points after the transformation, Σ_w is multiplied with the mean variance $\bar{s_o}^2 = s_O^2$ divided by the number of markers N_F.

To test if suitable markers were chosen, the transformation is calculated again with a different set of markers, resulting in a different $\hat{m}$ and $\vec{t}$. If the deviations are especially large ($>50\,\%$ of the mean) when using a certain set of markers, one (or more) of them should be replaced. The same is true, if the calculated transformation matrix differs significantly from the form given by Eq. (12). If false assignments were made between fiducial markers, this is also visible when looking at $\bar{d}$, since in this case $\bar{d}$ will be considerably larger than the uncertainties of the single coordinates.

Finally, the output is generated by the software, both as a text file containing the coordinates and error information and in form of the overlay images as described in section 4.1.2. In addition to the standard output, sections through the overlays can be displayed for monitoring purposes, see Appendix A.3.

4.3. Proof-of-principle

Introduction. For the development of the technique, quantum dots are used both as fiducial markers and as labels to be localized. Therefore, the position of all features is known by looking at the AFM image alone, compare also [16], and hence each point could be used either as fiducial marker or as a label. In this situation, no additional information can be gained by applying this technique, of course. In a productive application of this method — as opposed to the development — the positions of at least some fluorophores can not be extracted from the AFM image alone. That is the case, for example, if later smaller organic fluorophores are used as protein labels and quantum dots as fiducial markers only. To imitate such a situation, in the following examples only a subset of the quantum dots is chosen to function as fiducial markers, while the others serve only as labels, i.e. their positions are not determined in the AFM image, but only in the optical one. Subsequently, two images are shown demonstrating the application of the technique.

Methods. One sample on mica and another one on glass are shown. For the first, $16\,\mu$l of a $100\,$pM quantum dot suspension were deposited on mica, $35\,\mu$m thick. For the latter $18\,\mu$l of a $80\,$pM quantum dot suspension were deposited on glass. The preparation of the samples was performed according to section 3.1.

Results. Fig. 19 shows the raw fluorescence and AFM image of the sample on mica. For this experiment, 7 randomly selected fluorescent signals were localized in 16 images, resulting in a precision of the superlocalization of $s_O = 7.9\,$nm. The AFM pixel resolution is $7.8\,$nm/px and thus $s_A = 3.9\,$nm. Using the features encircled in Fig. 19 as fiducial markers, $\bar{d}$ is $5.2\,$nm and the total registration accuracy s_R is evaluated to: $s_R = 10.2\,$nm. Furthermore, Fig. 19 illustrates the advantage of the custom-designed output format, compared to a conventional fluorescence overlay. Finally, in Fig. 21 some enlarged details are shown to present the colocalization of the registered data.

Another example is shown in Fig. 20, where 5 randomly selected fluorescent signals were localized in 7 images, resulting in a precision of the superlocalization of $s_O = 5.4\,$nm. The total registration accuracy s_R is evaluated to: $s_R = 6.6\,$nm. In Fig. 20 the source images (with fiducial markers) and the overlay image is shown again. Additionally, the fitted positions of the labels are colour-coded in a 3D-representation of the topography. Before an example of a biological application of the technique is presented in chapter 5, accompanying simulations will be discussed in the following section, to further evaluate this technique.
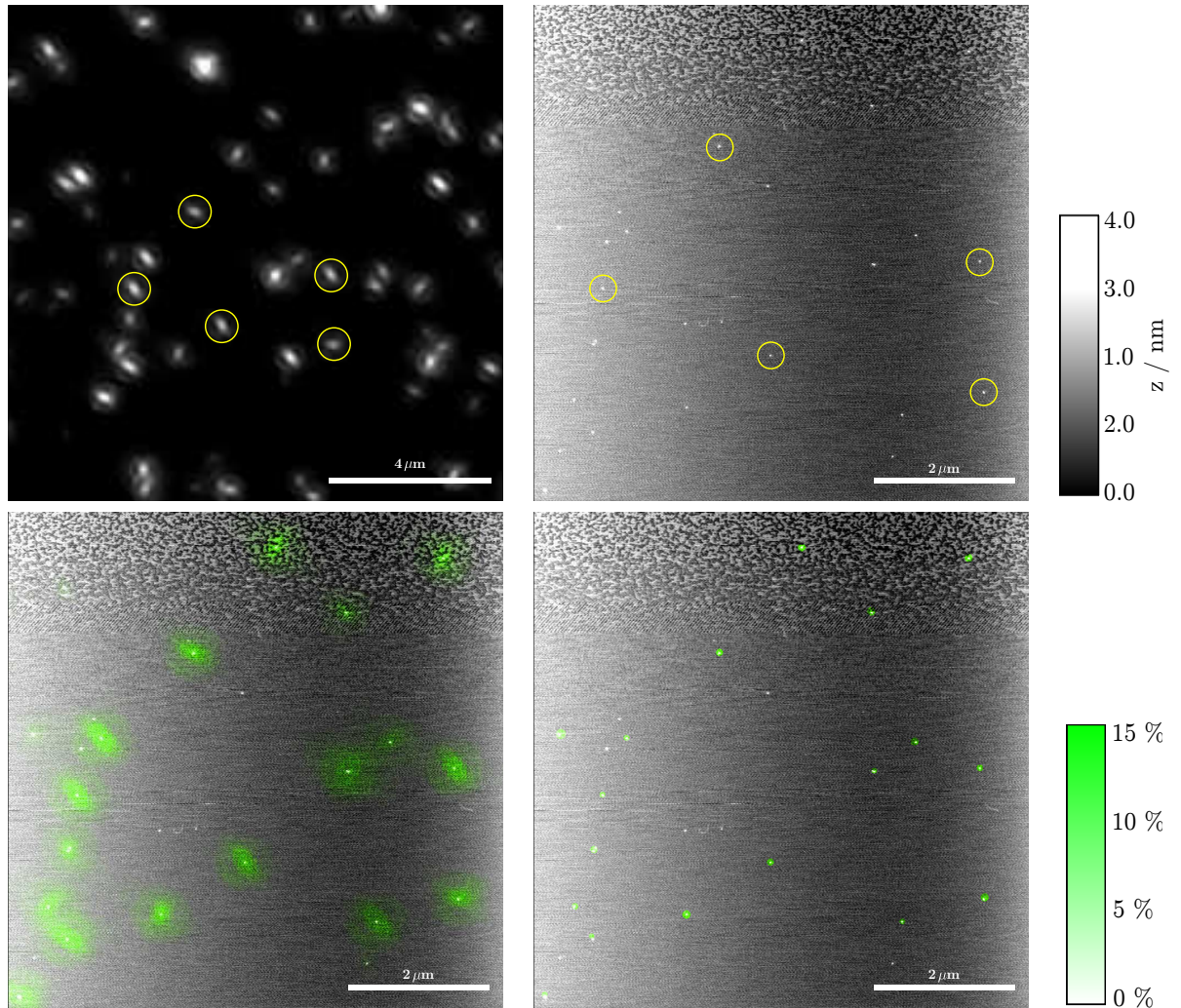
Fig. 19: Top row: Optical image (left) and AFM image (right) of a sample with quantum dots on mica (thickness: $35\,\mu$m). Circles indicate the spots used as fiducial markers. Bottom row: Combined Fluorescence and AFM image (left) and a computer generated overlay, depicting the probability density of the fluorophores' centres (right). In the optical image, the full scale is corresponding to $\zeta = 237$ photons/px.
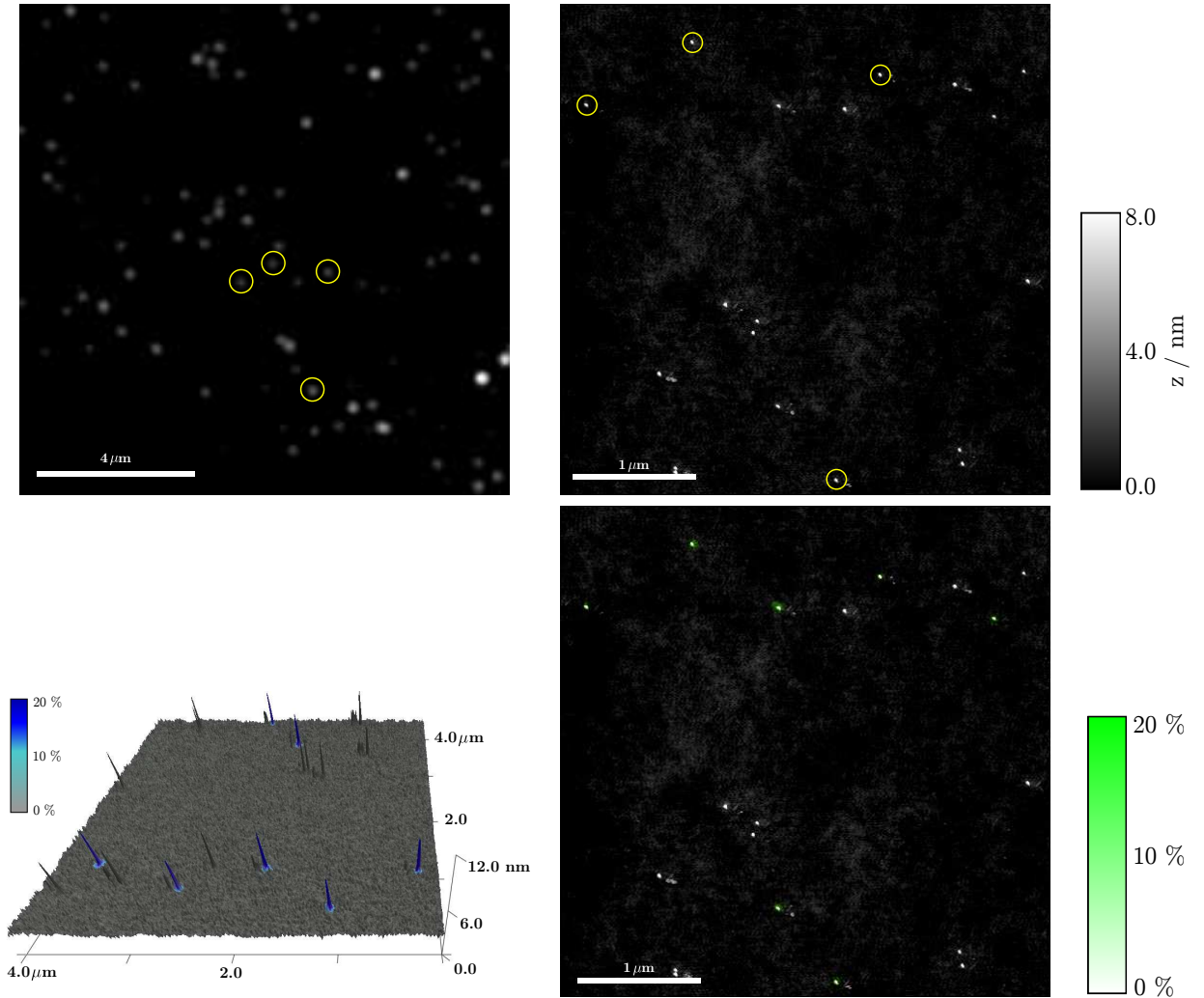
Fig. 20: Top row: Optical image (left) and AFM image (right) of a sample with quantum dots on glass. Circles indicate the spots used as fiducial markers. Bottom row: A 3D-representation of the surface (left) and the superlocalized positions of the fluorophores on top of the AFM image (right). The colour-code represents the probability of finding the centre of a fluorophore in the given pixel. The AFM pixel resolution is $7.8\,\mathrm{nm/px}$, the full scale in the optical image is corresponding to $\zeta = 262$ photons/px.
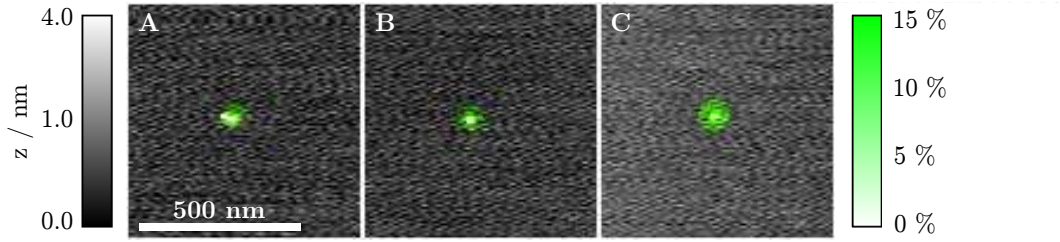
Fig. 21: Enlarged details of Fig. 19, showing some quantum dots that were not used as fiducial markers. The superlocalized positions (colour) and quantum dots colocalize perfectly within the given error margins.

4.4. Simulations

4.4.1. Introduction

Over the last decades computer power has increased dramatically. As a result, computer simulations have become an integral part of physical investigations. Compared to a purely theoretical approach they allow for a broader range of applications, even if the underlying problems can't (yet) be solved analytically. Compared to an experimental approach, simulations provide complete control of the "environment" and full knowledge of all relevant parameters. They require no expensive or hazardous material and, even though simulations may take longer than the actual measurement, usually they save a lot of time since they don't require sample preparation or tuning of instruments.

A simulated experiment can't fail in the sense of not being reproducible, but special care has to be taken to ensure the validity of the simulated results. Thus, not only the correct algorithm for a given problem has to be selected or created diligently, but it is just as important to know its limitations. In the end, the results obtained by a simulation have to be confirmed, typically by conducting a real experiment. During this thesis, the simulation code evolved in parallel with the analysis code and was mainly used for validation and control purposes. Nevertheless, some interesting conclusions can be drawn from the simulated data as demonstrated in the following sections.

4.4.2. Implementation

Pairs of artificial AFM and optical images were generated by the code shown in Appendix A.4. Similar programs already exist [15, 26], at least for the optical
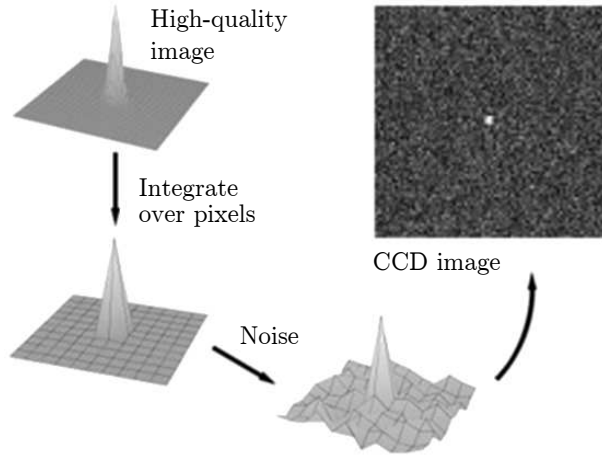
Fig. 22: Illustration of the image generation process. Adapted from [26].

part, nevertheless, the code was developed from scratch. Generation of the optical images is performed as described in [26] and basically involves three steps: Firstly, 2D-Gaussian shaped spots are added to a uniform background at random positions, secondly, the brightness values are discretized to a finite number of pixels and thirdly, Poissonian noise is added to each pixel. The process is illustrated in Fig. 22. By default, optical images were simulated with $512 \times 512 \, \text{px}^2$ and a resolution of $62.5 \, \text{nm/px}$, corresponding to the images captured by the experimental setup at full magnification. Eq. (4) describes the form of the fluorescent spots; typically their width s_g was chosen to be a few pixels and g_{max} corresponding to 90 % of the full brightness. Other parameters that can be adjusted in the simulation include the abundance of the spots, the background noise and the size and resolution of the AFM image.

The corresponding artificial AFM images are created by simply adding white pixels on a black background at the positions closest to each feature's centre. All properties of the AFM data except for its pixel resolution are ignored by this approach. This should be a valid simplification, though, since the analysis of the AFM images is not the critical part of this technique and the corresponding "local maximum detection" is a far more robust algorithm that does not need to be evaluated for that purpose.

The simulated images were then analyzed using the same software routine as for the experimentally obtained images, described in section 4.2. An accompanying text file is generated with each pair of simulated images, that contains information about the positions, resolution, transformation parameters, etc. This file can then be im-

ported again by the analysis software, see Appendix A.4 for an example. The actual simulation code is written as a *Mathematica* script and computations were performed on the CIP pool computers of the physics department, running *Mathematica 6.02*.

4.4.3. Code validation & results

First of all, the validity of the simulations has to be confirmed. Since the simulated data is subsequently used to validate the analysis algorithm, it cannot be itself validated by the same software. Instead, the simulated data was compared to images obtained experimentally using standard image analyzation software, such as *ImageJ* [56]. Analyzed are the background distribution and, most importantly, the size and form of the fluorescent spots.

The background distribution is varying among different images, depending on the exposure time, gain settings and substrate chosen. Nevertheless a good agreement with the simulated data can be achieved in most cases, see Fig. 23 for an example. The shape of the fluorescent spots was compared to experimental data by looking at cross sections through the peaks' centres in the experimental images. The signal shape is in excellent agreement with the experimental data, see Fig. 24. The images produced by the simulation code are thus considered valid, making it possible to use them for testing the correctness of the analyzation code and for evaluating its performance.
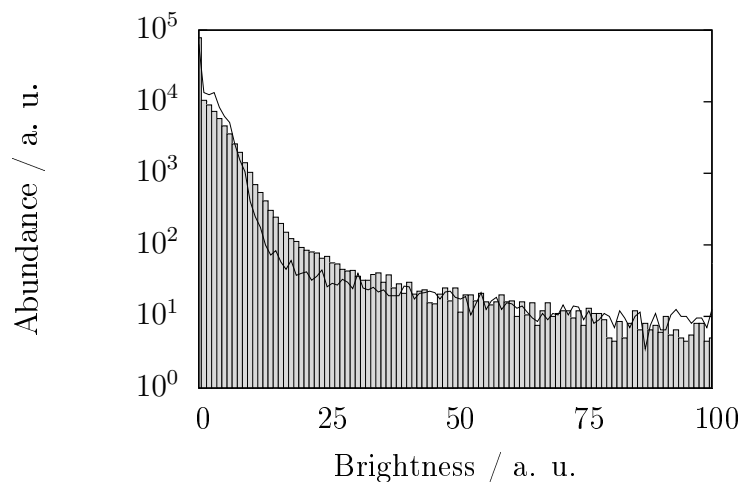

Fig. 23: Histogram of a typical fluorescent image (exposure time: $800\,\mu$s) and background distribution of an artificial image simulated accordingly (line).
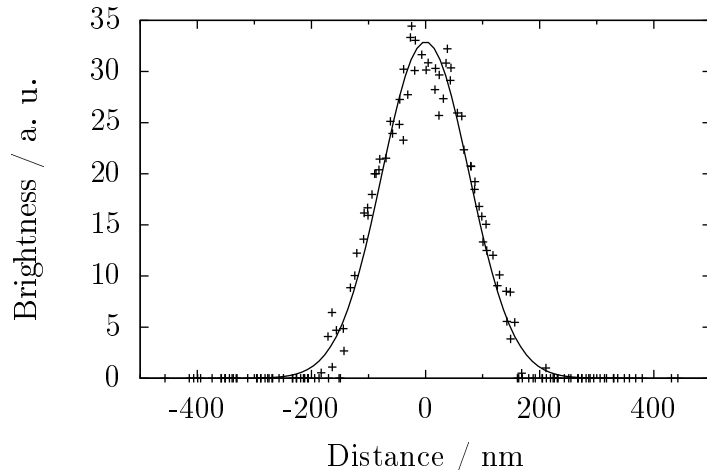
46

Fig. 24: Comparison of the experimental (points) and simulated peak form (line). The data was obtained from sections through $N = 12$ peaks in a fluorescent image of quantum dots on a glass substrate. Centres are aligned and the height normalized.

Validity of the analyzation code. Next, simulations are used to validate the registration algorithm. In order to check its reliability, both the coordinates it outputs and the corresponding error margins were checked against the true coordinates that are precisely known for simulated images. In Fig. 25 an example is shown, where the error calculated by the registration software (as described in section 4.2) is compared to the actual distance between matching points after the registration. Even though the error indicated by the software turns out to be slightly larger than the actual mismatch, especially for smaller SNR, it clearly indicates the correct order of magnitude and does in no case underestimate the error.

Additionally, different signal shapes were simulated, mimicking the effects observed when imaging on mica substrates. Firstly, an elliptical distortion of the signal was simulated by choosing different values for $s_{g,x}$ and $s_{g,y}$ in Eq. (4) when generating the optical images. Secondly, the effect of fitting a non-Gaussian shaped signal with a Gaussian function was tested by altering the code to generate peaks with the following quadrupole-like form

$$q\left(x, y\right) = q_{max} \cdot \sum_{i=1}^{4} \frac{w_q}{\sqrt{\left(x - x_i\right)^2 + \left(y - y_i\right)^2}} \, . \tag{23}$$

Here, w_q is the width of the quadrupole and x_i, $y_i = \pm 1 \, \text{px}$. The singularity at $(x, y) = (x_i, y_i)$ has to be taken care of, but this can be done by clipping all values
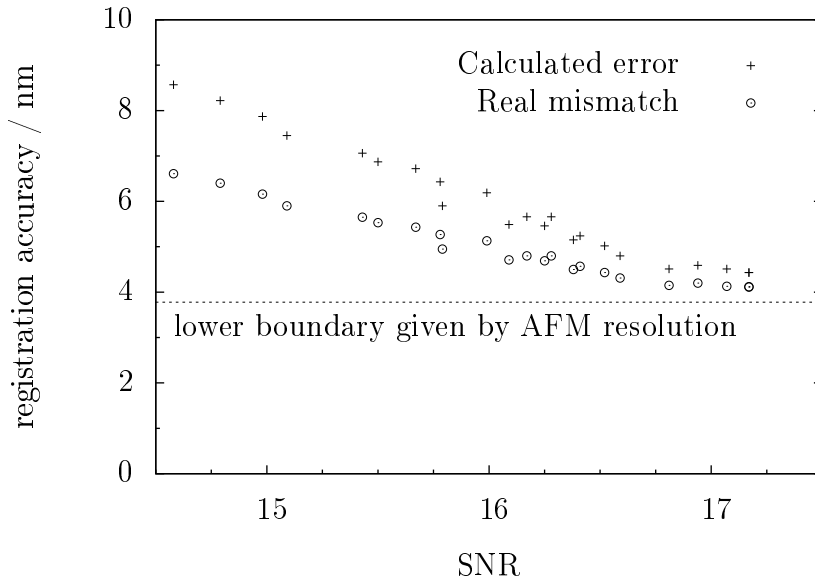
Fig. 25: Registration results for varying SNR and/or background noise. Shown are the errors output by the analysis software (crosses) and the actual distances of corresponding simulated points after the registration (circles). Simulation parameters: $g_{max} = 300$, $s_g = 3.5\,\mathrm{px} \approx 200\,\mathrm{nm}$, $r_A = 7.6\,\mathrm{nm}$.

above a certain threshold. The results can be seen in Figs. 26 and 27. While the elliptic distortions do not affect the quality of the fitting (when using sufficiently large ROIs, see below), the quadrupole-like signals are fitted considerably less precise. Even though these shapes do not reflect the real form of the distorted signals, this simulation shows that fitting an arbitrary symmetrical signal form with a Gaussian is possible and that the precision still increases with the SNR.

Finally, the influence of the placement of the regions of interest (ROIs) around the fiducial markers is investigated. This checkup is necessary since the placement of these ROIs is done by hand and are therefore prone to variations. For this analysis, simulated images made up of perfectly Gaussian shaped spots and elliptically distorted spots are used. Superlocalization is applied multiple times to each image, with the ROIs placed slightly differently each time. The results are shown in Table 4. The first column is obtained by shifting all ROIs by $1\,\mathrm{px}$ to the right (relative to the perfectly centred position). For the second column, each ROI was moved by a random offset in between $-2\,\mathrm{px}$ and $+2\,\mathrm{px}$ in $x-$and $y-$direction, respectively. This interval roughly corresponds to the accuracy in the placement by hand. Looking at Table 4, it can be seen that for the undistorted optical images, the influence of the ROI placement is several times smaller than the precision achieved by the
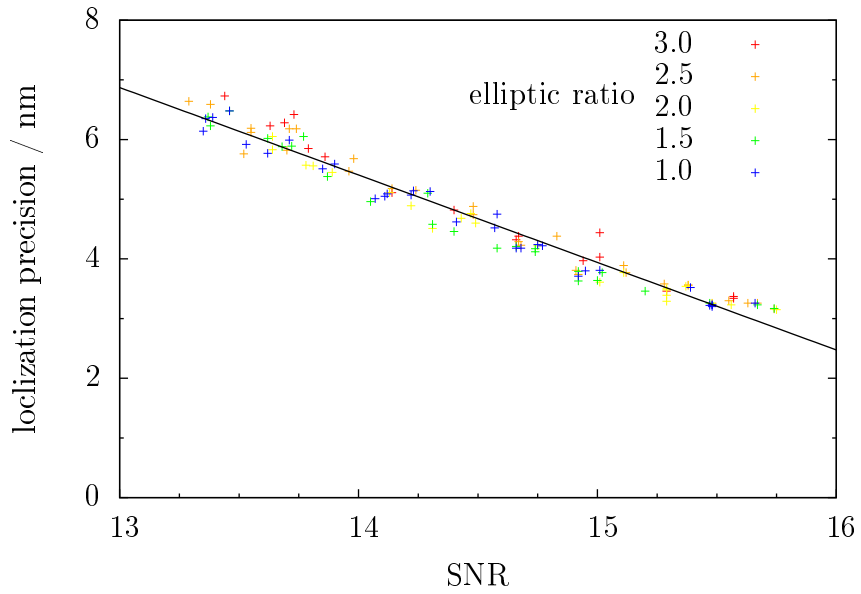
Fig. 26: Influence of distorted signal shapes on the superlocalization. The precision for simulated peaks with different elliptic distortion is compared. Simulation parameters: $g_{max} = 210$, $s_{gx} = 4.25\,\mathrm{px} = 266\,\mathrm{nm}$, $r_A = 7.6\,\mathrm{nm}$.
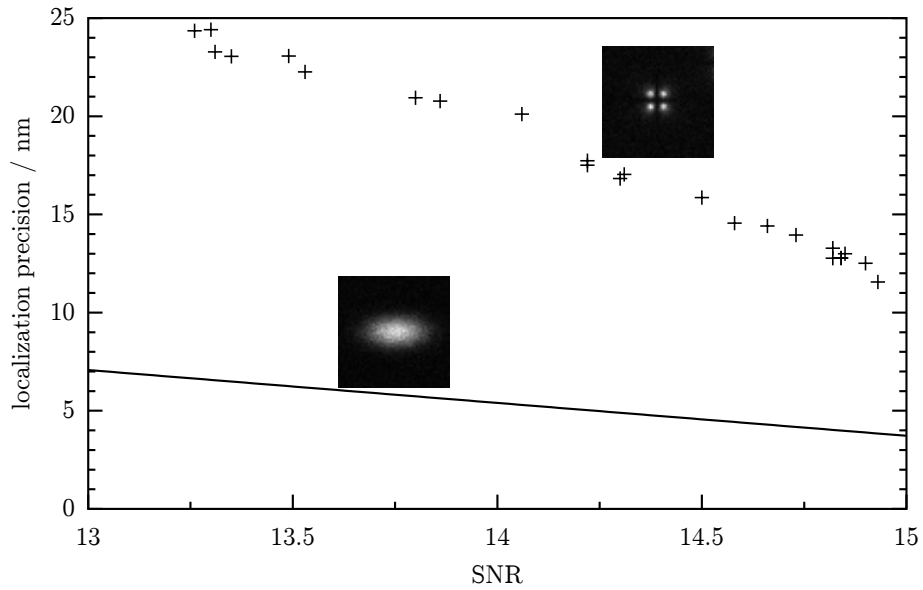
Fig. 27: Influence of distorted signal shapes on the superlocalization. The precision for quadrupole-like distorted signal shapes is shown as points. The line is identical to the one in Fig. 26, i.e. fitted to the localization precision in the presence of elliptical distortions. Insets depict the simulated signal shapes. Simulation parameters: $q_{max} = 210$, $w_q = 1\,\mathrm{px} = 62.5\,\mathrm{nm}$, others as in Fig. 49.

superlocalization and can hence be neglected. For the elliptical shaped signals, the difference reaches and often exceeds the fitting precision. The major contribution to this difference is due to the size of the ROI, though. Deformed signals can be spread over an area many times larger than the size of a perfectly focused spot, cf. Fig. 12 on page 28. If the ROI is too small, the rim of the signal is cut off and thereby information is lost. If the ROI size is increased, this effect can be alleviated, as shown in the third row of Table 4. In this example the ROI was resized from $20 \times 20 \, \text{px}^2$ to $40 \times 40 \, \text{px}^2$.

Finally, the simulations can be used to show what signal quality the experimental images have to reach in order to achieve the desired precision when locating the fluorophore centres. For that purpose, a wider range of SNR was simulated, roughly matching the range of experimental conditions, by varying the background intensity. Using the results shown in Fig. 28, the registration accuracy to be expected can be determined beforehand for similar experiments.

| | ROI position (relative to perfectly centred) | | |
	constant offset +1 px	random offset ±2 px	positional precision
perfect Gaussian	0.09	0.11	3.5
elliptic	21	24	4.1
el. with larger ROI	0.73	0.77	3.9

Table 4.: Displacement of the superlocalized positions when fitted with an imperfectly centred ROI. The table shows the mean distance by which the calculated centre of a fluorescent signal is shifted when the corresponding ROI is placed off-centre. The effect is shown for a perfect Gaussian and an elliptic signal shape, the latter fitted with a large and standard ROI size. The precision by which the positions can be determined is shown for comparison. All values in nm.
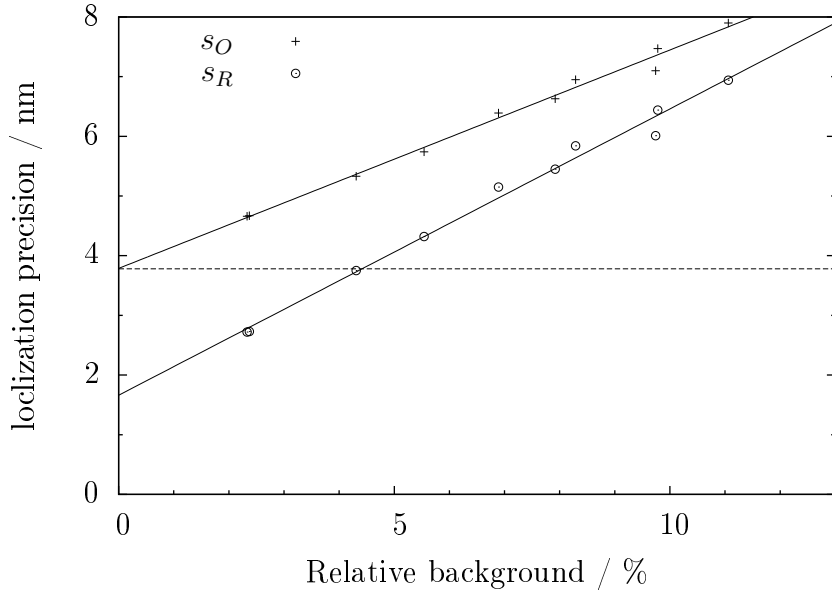
Fig. 28: Superlocalization precision s_O (crosses) and total registration accuracy s_R (circles) for simulations with varying relative background noise. For low noise, the limitation given by the AFM resolution (dashed line) becomes more important. Simulation Parameters: $g_{max} = 210$, $s_g = \text{Random}[2, 2.5] \approx 350\text{–}440\,\text{nm}$, $r_A = 7.6\,\text{nm}$. The data was generated with a former version of the simulation software, which calculated the background intensity relative to the signal height instead of the SNR as defined in Eq. (6).

5. Biological Application

Finally, to show the prospects of this new technique, it is applied to a biological system. As an example, the damage recognition system of the prokaryotic nucleotide excision repair (NER) system was chosen. Quantum dots are used both as fiducial markers and as protein labels.

5.1. Damage recognition in NER

NER is one of a number of DNA-repair mechanisms present in all living cells. The proteins involved scan the DNA for potential damages, verify them and repair them, see p. 192ff in [58]. It acts on a variety of DNA lesions and adducts, compiled for example in [59]. In humans, the homologous system is the only means of removing damages induced by UV radiation. Malfunction of NER is related to the disease *Xeroderma pigmentosum* (among others, see [60]) and even though the eukaryotic NER is more complicated and involves more types of proteins, new insights can be gained about the human system by studying its bacterial counterpart [61].

In the prokaryotic NER, damage recognition and verification is performed by two proteins, named UvrA and UvrB. UvrA is a $\sim 103\,\text{kDa}$ protein, that can bind and move along the DNA. UvrB is a $\sim 75\,\text{kDa}$ protein and the central protagonist in bacterial NER, that likely verifies potential lesions and initiates the consecutive repair process [62]. For this work, purified wild type proteins from *Bacillus caldotenax* are used.

The proposed steps of the reaction in vivo are shown in Fig. 29. Firstly, UvrA forms a dimer in solution and is then believed to be joined by two molecules of UvrB. This complex attaches to and walks along the DNA until a potential damage is found. The conformation of the complex is then changed and in case the lesion is verified, the DNA strands are partially separated and the so-called preincision complex is formed, consisting of the DNA wrapped around one molecule of UvrB at the damage site [64]. The other proteins detach from the DNA. While this model is generally agreed upon, the composition of the scanning complex of UvrA and
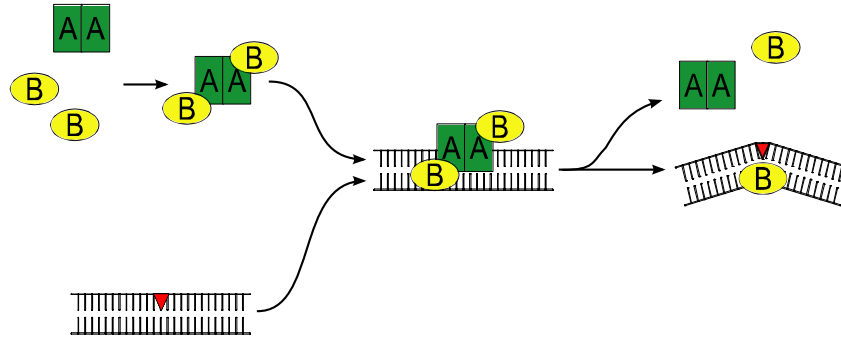
Fig. 29: Proposed mechanism of the damage recognition steps in NER. A = UvrA, B = UvrB, ▼ = DNA damage. Adapted from [63].

UvrB is yet subject to discussion, proposed models being a $UvrA_2B_2$ or a $UvrA_2B_1$ complex. For a more profound and detailed description of the bacterial NER system, see [59, 62].

UvrB can be conjugated to quantum dots (QDs) using a secondary antibody reaction [16]. For this, a UvrB variant with a hemagglutinin (HA) epitope tag added to its N-terminal end is used. The UvrB-QD conjugate is shown in Fig. 30. The protein retains its function in the context of NER despite the attached QD, see [16].
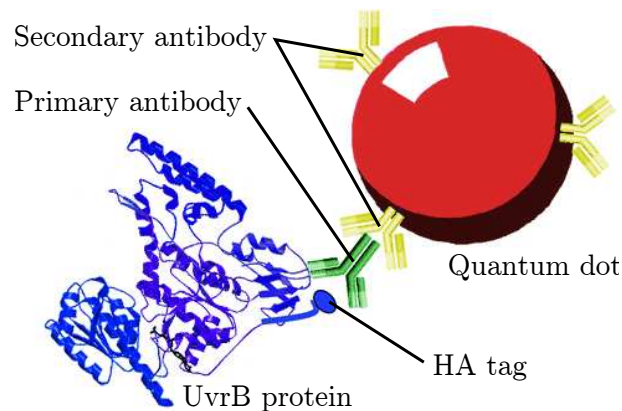
Fig. 30: Structure of the UvrB-Quantum dot conjugate (figure not to scale). Adapted from [16].

UV-damaged DNA prepared by H. Wang (University of Pittsburgh, PA, USA) is used as a substrate for NER. That DNA originates from the phage λ virus, is 48502 base-pairs in length and contains 3–5 damages per molecule. This long DNA has the advantage of being prominently visible even in larger AFM images. The damages present are cyclobutane pyrimidine dimers, most typically thymine-thymine-dimers [24]. This type of damage is recognized by NER with high specificity.

5.2. Sample preparation

The UvrB-QD conjugate is prepared beforehand and can be stored for several days at 4°C. To produce it, a monoclonal HA antibody (from mouse) is incubated for one hour at room temperature with the HA tagged protein at a 1:1 molar ratio, before adding the QDs, coated with the secondary anti-mouse antibodies. To ensure that only one protein is bound to a QD and that no UvrB molecules remain unbound, the incubation is carried out at a 4–5 fold excess of QDs. The results of the UvrB-QD conjugation are tested by recording AFM images with the conjugate deposited at a high concentration of $\sim 15\,\text{nM}$.

Samples are prepared by incubating the components at concentrations of 10^{-6}–$10^{-8}\,\text{mol/l}$ for 10–20 minutes in binding buffer (see Appendix A.2) at room temperature to allow for the damage recognition to proceed. A fraction of the incubation is then diluted in the deposition buffer (see Appendix A.2) to a final concentration in the high picomolar range. UvrA and DNA were added according to the expected stoichiometric concentrations. For the sample, discussed below, a total volume of $2.0\,\mu l$ containing $10.5\,\text{nM}$ of λ-DNA, $39.0\,\text{nM}$ of quantum dots (approx. $20\,\%$ conjugated to UvrB) and $7.8\,\text{nM}$ of UvrA in binding buffer was incubated at room temperature for $11\,\text{min}$. The deposition on a mica substrate is then carried out with a $100\times$ dilute solution as described in section 3.1.

A general review of sample preparation methods for biological AFM imaging can be found in [65].

5.3. Results

Fig. 31 shows the result of a QD-UvrB conjugation. Both conjugated and unconjugated QDs are counted in several images, indicating the fraction of the QDs bound to UvrB. In the assay shown in Fig. 31, $(9.2 \pm 5.5)\,\%$ of the total QDs are attached to a protein. The uncertainty arises form the fact that some UvrB molecules are arranged below the QDs making it hard to tell for certain whether a particular QD is conjugated or not. All conjugations performed for this work were successful, even though the efficiency varied and was not always explicitly examined.

Next, the biological system consisting of UvrA, UvrB-QD and the damaged DNA is examined. Fig. 33 shows the topography and fluorescence of the sample as well as the composite image revealing the positions of the fluorescent labels in the AFM image. Looking at the AFM images alone, different complexes corresponding to
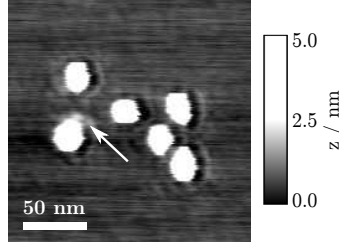
Fig. 31: AFM image of a conjugated quantum dot among unconjugated ones. The UvrB molecule is marked with an arrow.
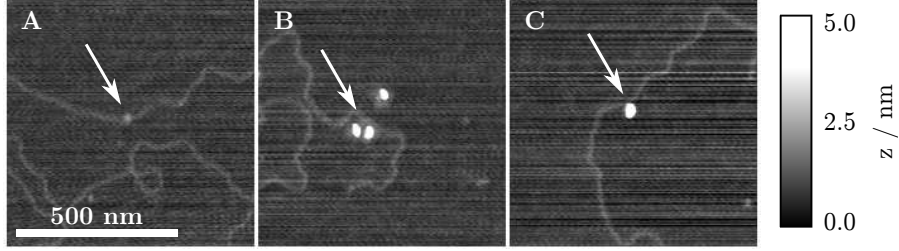

Fig. 32: Topographical details the sample. Different types of complexes attached to the DNA are shown, likely consisting of UvrA alone (**A**) , the scanning complex $UvrA_2B_2$ (**B**) and the preincision complex, UvrB alone (**C**). All UvrB molecules are attached to quantum dots. The z-scale is slightly oversaturated to make the low features better visible.

the different steps of the damage recognition can be identified (enlarged details in Fig. 32). N.B. the complexes present in this image can be used to support the hypothesis of a $UvrA_2B_2$ scanning complex, cf. [59].

From the optical images (23 were captured of that region), 7 peaks were randomly chosen and tracked across all images, yielding a precision of $s_O = 7.8$ nm for the fitted positions. The AFM pixel resolution r_A is 3.9 nm/px, thus $s_A = 2.0$ nm . Using the peaks encircled in Fig. 33 as fiducial markers, the registration was performed, resulting in a mean distance of matching fiducial markers after the transformation of $\bar{d} = 3.5$ nm. The overall accuracy of the registration evaluates to $s_R = 8.8$ nm, which is sufficient to identify single molecules in the image.

Fig. 34 depicts an interesting situation, where only one QD out of two in a complex is optically active (determined by shape and brightness of the fluorescent signal). Looking at the fluorescence alone, it is impossible to assign the signal to one of the molecules. However, using the superlocalization technique, the source of the fluorescence can be clearly identified. Although the superlocalized fluorescence only indicates the positions of the QDs in this example, which are known anyway from the AFM image, it clearly shows the reliability and power of this technique. As

a possible extension, the use of smaller organic fluorophores, invisible by AFM, is discussed in the following outlook.
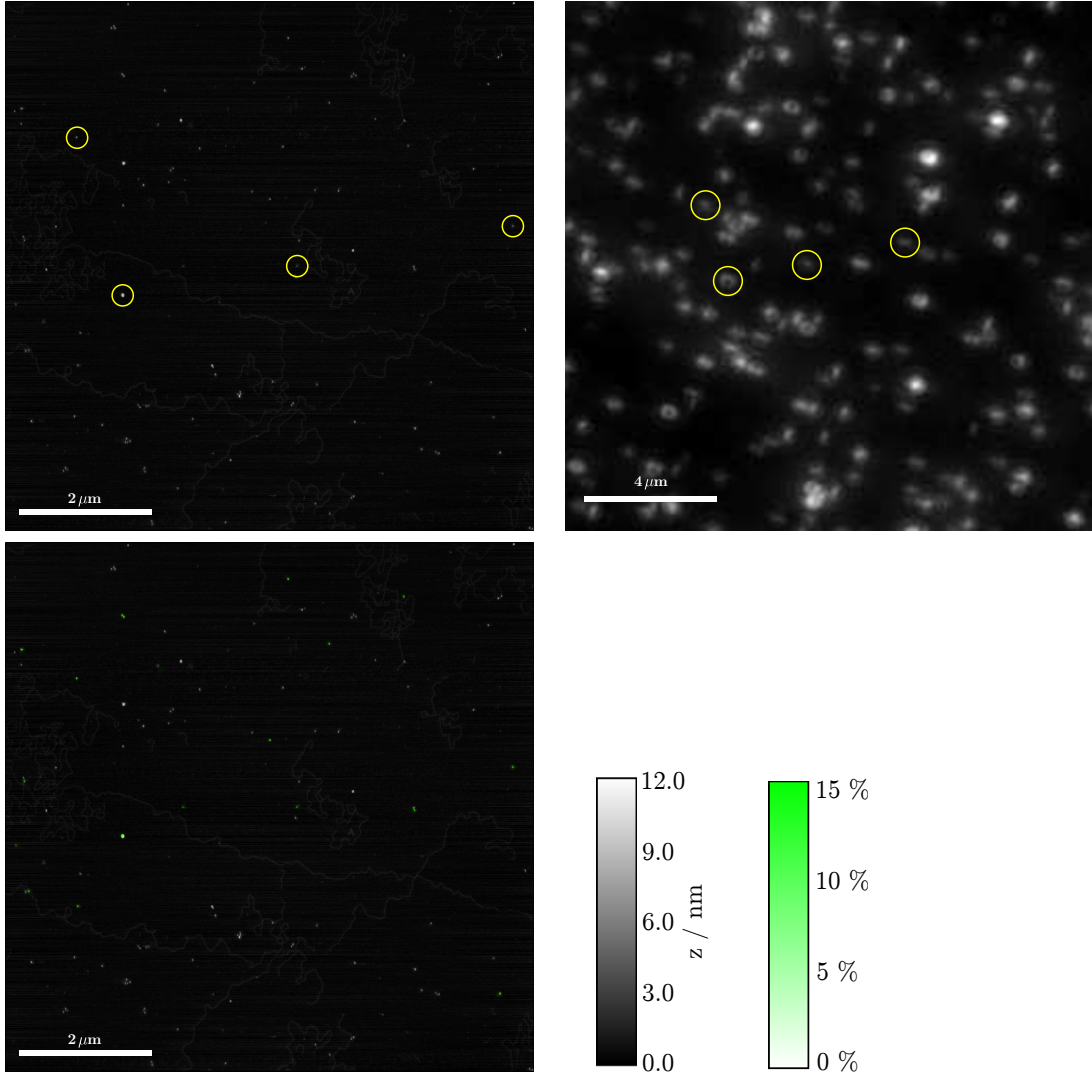
Fig. 33: Top row: AFM image (left) and optical image (right) of a sample with UV-damaged DNA, UvrA and UvrB-QD on mica. Circles indicate the spots used as fiducial markers. In the optical image, the full scale is corresponding to $\zeta = 335$ photons/px. Bottom row: Overlay of the topography and the superlocalized label positions (colour). Registration accuracy: $s_R = 8.8$ nm. The fitted centres of fluorescence almost perfectly colocalize with the quantum dots.
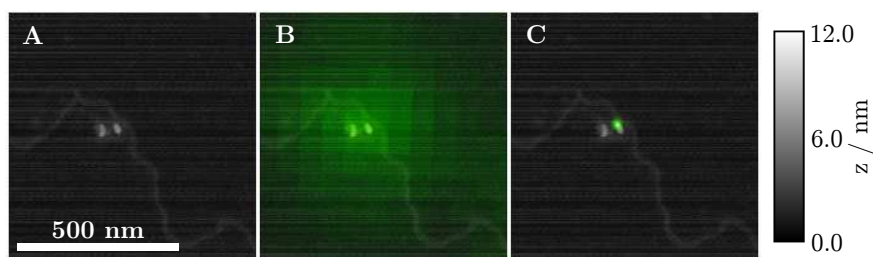
Fig. 34: Enlarged detail, showing a complex containing two UvrB-QD conjugates, one of them optically inactive. Shown is the topography only (**A**), the topography with the aligned fluorescence signal (**B**) and with superlocalization applied (**C**).

6. Conclusion & Outlook

Summary.   Within the scope of this work, an imaging method was developed, combining atomic force microscopy and superlocalization of single molecule fluorescence, capable of identifying single labelled proteins in AFM images. An experimental protocol for sample preparation and data acquisition was established. Software for data analysis and image registration was programmed and evaluated using both simulated and measured data. A survey of the experimental results as well as theoretical considerations provide an assessment of the accuracy with which the individual positions can be determined. The method was applied to localize quantum dots in AFM images, both on their own and in a biological context. A registration accuracy of less than 10 nm could be realized, demonstrating that the identification of single molecules is possible using this method. Nevertheless, further improvements are to be expected and shall be briefly discussed in the following outlook.

Technical advancements.   An likely advancement is the availability of even better substrates. Even though a perfect material is not known to the author, possible candidates that could improve the performance of this technique even further are sapphire [66] and minerals of the mica group with lower birefringence and more suitable refraction indexes, e.g. Illite (a.k.a. white mica) [67]. Recent advances in the development of AFM allow for dramatically increased scanning speeds [3, 68] bringing the time resolution to the edge of live imaging. When imaging in liquid, the biological systems can be kept in an active state [3] and it may then be possible to watch labelled proteins in action. Even better noise decoupling — or the use of a camera cooled without movable parts — would then allow for simultaneous AFM and optical imaging [46]. On the computational side, the need for human interaction during the analysis has to be reduced, thereby standardizing the technique and making it more "user-friendly". Especially, some form of automated quality control is required for this.

Smaller fluorophores. The most promising extension of the technique is the use of smaller, organic fluorophores as protein labels instead of quantum dots. A comprehensive review of the fluorophores available for biological imaging and their advantages can be found in [7]. A good example would be *Alexa Fluor*, see p. 69ff in [5], that can be covalently attached to specific residues of a protein. Firstly, the proteins are virtually unaffected in their function and binding properties by the small additions. Secondly, the regions of interest can be seen better in the AFM images, since no voluminous markers are nearby or even on top of the proteins to be investigated. Quantum dots would still be used as fiducial markers, i.e. for calculating the transformation in the registration process, of course. Compared to quantum dots, most organic fluorophores show a reduced fluorescent response and suffer more from photobleaching, cf. p. 768ff in [5]. However, if great care is taken to collect the majority of the photons emitted, the intensity should be sufficient for superlocalization, compare [12].

Multi-colour labelling. Another interesting option is the possibility to use more than one type of fluorescent marker and take images using different filter sets. On the one hand, the fiducial markers could have another colour than the protein labels, facilitating the "raw alignment" described in section 2.2.3. As long a the light path isn't affected by changing the filter sets, the transformation calculated using the fiducial markers can be applied without modification to the image containing the fluorescent signal of other dyes. That way, the coverage of both the markers and the objects of investigation can be optimized independently and thereby significantly increased, without risking to have too many overlapping spots that could otherwise not be fitted properly. On the other hand, more than one type of protein could be labelled simultaneously, allowing for different proteins to be localized within one and the same AFM image, even if they are very close to each other.

These ideas, many of them novel as of today, show that the advancement of this integrated AFM/fluorescence superlocalization technique has great potential. Therefore it can be called a promising technique that will hopefully soon expediently expand the range of methods available to the biological researcher.

Acknowledgements

Bibliography

[1] G. Binning, C. F. Quate, and C. Gerber. *Atomic Force Microscope.* Physical Review Letters **56**, 930–933 (1986).

[2] Y. Seo and W. Jhe. *Atomic force microscopy and spectroscopy.* Reports on Progress in Physics **71**, 016101 (2008).

[3] J. K. H. Hörber and M. J. Miles. *Scanning Probe Evolution in Biology.* Science **302**, 1002–1005 (2003).

[4] C. C. Friedel and R. Zimmer. *Identifying the topology of protein complexes from affinity purification assays.* Bioinformatics **25**, 2140–2146 (2009).

[5] J. R. Lakowicz. *Principles of fluorescence spectroscopy.* Third edition. Springer (2006).

[6] A. Gaiduk, R. Kühnemuth, S. Felekyan, M. Antonik, W. Becker, V. Kudryavtsev, C. Sandhagen, and C. A. M. Seidel. *Fluorescence detection with high time resolution: From optical microscopy to simultaneous force and fluorescence spectroscopy.* Microscopy Research and Technique **70**, 433–441 (2007).

[7] B. N. G. Giepmans, S. R. Adams, M. H. Ellisman, and R. Y. Tsien. *The Fluorescent Toolbox for Assessing Protein Location and Function.* Science **312**, 217–224 (2006).

[8] D. W. Pohl, W. Denk, and M. Lanz. *Optical stethoscopy: Image recording with resolution lambda/20.* Applied Physics Letters **44**, 651–653 (1984).

[9] E. Betzig, A. Lewis, A. Harootunian, M. Isaacson, and E. Kratschmer. *Near Field Scanning Optical Microscopy (NSOM): Development and Biophysical Applications.* Biophysical Journal **49**, 269–279 (1986).

[10] T. A. Klar, S. Jakobs, M. Dyba, A. Egner, and S. W. Hell. *Fluorescence microscopy with diffraction resolution barrier broken by stimulated emission.* Proceedings of the National Academy of Sciences of the United States of America **97**, 8206–8210 (2000).

[11] E. Betzig, G. H. Patterson, R. Sougrat, O. W. Lindwasser, S. Olenych, J. S. Bonifacino, M. W. Davidson, J. Lippincott-Schwartz, and H. F. Hess. *Imaging Intracellular Fluorescent Proteins at Nanometer Resolution.* Science **313**, 1642–1645 (2006).

[12] A. Yildiz, J. N. Forkey, S. A. McKinney, T. Ha, Y. E. Goldman, and P. R. Selvin. *Myosin V walks hand-over-hand: single fluorophore imaging with 1.5-nm localization.* Science **300**, 2061–2065 (2003).

[13] A. Yildiz and P. R. Selvin. *Fluorescence Imaging with One Nanometer Accuracy: Application to Molecular Motors.* Accounts of Chemical Research **38**, 574–582 (2005).

[14] N. Bobroff. *Position measurement with a resolution and noise-limited instrument.* Review of Scientific Instruments **57**, 1152–1157 (1986).

[15] R. E. Thompson, D. R. Larson, and W. W. Webb. *Precise Nanometer Localization Analysis for Individual Fluorescent Probes.* Biophysical Journal **82**, 2775–2783 (2002).

[16] H. Wang, I. Tessmer, D. L. Croteau, D. A. Erie, and B. Van Houten. *Functional Characterization and Atomic Force Microscopy of a DNA Repair Protein Conjugated to a Quantum Dot.* Nano Letters **8**, 1631–1637 (2008).

[17] G. Ekspong (Ed.). *Nobel Lectures in Physics 1981-1990.* Nobel Lectures in Physics. World Scientific Publishing Co. (1993). Including Presentation Speeches and Laureates' Biographies.

[18] J. K. H. Hörber, C. A. Lang, T. W. Hänsch, W. M. Heckl, and H. Möhwald. *Scanning tunneling microscopy of lipid films and embedded biomolecules.* Chemical Physics Letters **145**, 151–158 (1988).

[19] S. Morita, R. Wiesendanger, and E. Meyer (Eds.). *Noncontact Atomic Force Microscopy.* Springer (2002).

[20] Q. Zhong, D. Inniss, K. Kjoller, and V. B. Elings. *Fractured polymer/silica fiber surface studied by tapping mode atomic force microscopy.* Surface Science **290**, L688–L692 (1993).

[21] L. Henke, N. Nagy, and U. J. Krull. *An AFM determination of the effects on surface roughness caused by cleaning of fused silica and glass substrates in the process of optical biosensor preparation.* Biosensors and Bioelectronics **17**, 547–555 (2002).

[22] R. Fuierer. *MFP-3D Procedure Operation Manualette.* Asylum Research, Santa Barbara, CA 93117, 10th edition (Sep 2008).

[23] L. Novotny and B. Hecht. *Principles of Nano-Optics.* Cambridge University Press (2007).

[24] R. Beukers, A. P. M. Eker, and P. H. M. Lohman. *50 years thymine dimer.* DNA Repair **7**, 530–543 (2008).

[25] I. N. Bronstein, K. A. Semendjajew, G. Musiol, and H. Mühlig. *Taschenbuch der Mathematik*. Deutsch (Harri) (2000).

[26] M. K. Cheezum, W. F. Walker, and W. H. Guilford. *Quantitative Comparison of Algorithms for Tracking Single Fluorescent Particles*. Biophysical Journal **81**, 2378–2388 (2001).

[27] M. S. Robbins and B. J. Hadwen. *The noise performance of electron multiplying charge-coupled devices*. IEEE Transactions on Electron Devices **50**, 1227–1232 (2003).

[28] Hamamatsu. *ImagEM EM-CCD technical note* (2006). `http://sales.hamamatsu.com/index.php?id=13200389`.

[29] R. W. Watkins and C. R. Robertson. *Total internal-reflection technique for examination of protein adsorption*. Journal of Biomedical Materials Research **11**, 915–938 (1977).

[30] Olympus. *Research Inverted System Microscope IX71/IX81*. Olympus. `http://www.olympusamerica.com/seg_section/product.asp?product=1023&p=-1`.

[31] H. Herrmann (Hamamatsu). *Private Communication* (2009).

[32] W. Heisenberg. *Die physikalischen Prinzipien der Quantentheorie*. Hirzel, Leipzig (1930).

[33] R. J. Ober, S. Ram, and E. S. Ward. *Localization Accuracy in Single-Molecule Microscopy*. Biophysical Journal **86**, 1185–1200 (2004).

[34] C. M. Anderson, G. N. Georgiou, I. E. G. Morrison, G. V. W. Stevenson, and R. J. Cherry. *Tracking of cell surface receptors by fluorescence digital imaging microscopy using a charge-coupled device camera. Low-density lipoprotein and influenza virus receptor mobility at 4 degrees C*. Journal Of Cell Science **101**, 415–425 (1992).

[35] M. J. Rust, M. Bates, and X. Zhuang. *Sub-diffraction-limit imaging by stochastic optical reconstruction microscopy (STORM)*. Nature Methods **3**, 793–796 (2006).

[36] P. R. Bevington and D. K. Robinson. *Data Reduction and Error Analysis for the Physical Sciences*. Third edition. McGraw-Hill (2003).

[37] I. L. Medintz, H. T. Uyeda, E. R. Goldman, and H. Mattoussi. *Quantum dot bioconjugates for imaging, labelling and sensing*. Nature Materials **4**, 435–446 (2005).

[38] J.-M. Cocchi. *Quantum Dot Nanocrystals*. Invitrogen (2008). `http://microscopie.univ-rennes1.fr/doc-logiciels/DocsInvitrogen/02QuantumDotNanocrystalsPLATIM100408.pdf`.

[39] Invitrogen. *Qdot Secondary Antibody Conjugates*. Invitrogen - Molecular Probes (2007). `http://probes.invitrogen.com/media/pis/mp11001.pdf`.

[40] R. Dave, D. S. Terry, J. B. Munro, and S. C. Blanchard. *Mitigating Unwanted Photophysical Processes for Improved Single-Molecule Fluorescence Imaging.* Biophysical Journal **96**, 2371–2381 (2009).

[41] X. Brokmann, L. Coolen, J.-P. Hermier, and M. Dahan. *Emission properties of single CdSe/ZnS quantum dots close to a dielectric interface.* Chemical Physics **318**, 91–98 (2005). Molecular Nanoscience - In honour of Daniel S. Chemla on his 65th birthday.

[42] Mineral database (mindat.org). *Muscovite datasheet.* `http://www.mindat.org/min-2815.html`.

[43] S. Karrasch, M. Dolder, F. Schabert, J. Ramsden, and A. Engel. *Covalent binding of biological samples to solid supports for scanning probe microscopy in buffer solution.* Biophysical Journal **65**, 2437–2446 (1993).

[44] A. Gaiduk. *Steps towards simultaneous atomic-force and fluorescence spectroscopy of single DNA.* Ph.D. thesis, Heinrich-Heine-University Düsseldorf (2006).

[45] M. Sasou, S. Sugiyama, T. Yoshino, and T. Ohtani. *Molecular Flat Mica Surface Silanized with Methyltrimethoxysilane for Fixing and Straightening DNA.* Langmuir **19**, 9845–9849 (2003).

[46] H. Gumpp, S. W. Stahl, M. Strackharn, E. M. Puchner, and H. E. Gaub. *Ultrastable combined atomic force and total internal fluorescence microscope.* Review of Scientific Instruments **80**, 063704 (2009).

[47] R. Kassies, K. O. Van der Werf, A. Lenferink, C. N. Hunter, J. D. Olsen, V. Subramaniam, and C. Otto. *Combined AFM and confocal fluorescence microscope for applications in bio-nanotechnology.* Journal of Microscopy **217**, 109–116 (2005).

[48] L. G. Brown. *A survey of image registration techniques.* ACM Computing Surveys **24**, 325–376 (1992).

[49] J. Modersitzki. *Numerical Methods for Image Registration.* Oxford University Press (2004).

[50] J. X. Chen. *Guide to Graphics Software Tools.* Second edition. Springer (2008).

[51] K. Rohr. *Landmark-Based Image Analysis*, volume 21 of *Computational Imaging and Vision*. First edition. Kluwer Academic (2001).

[52] Y. Amit. *A Nonlinear Variational Problem for Image Matching.* SIAM Journal on Scientific Computing **15**, 207–224 (1994).

[53] W. Research. *Wolfram Mathematica 6* (August 2009). `http://www.wolfram.com/products/mathematica/newin6/`.

[54] N. Brandle, H. Y. Chen, H. Bischof, and H. Lapp. *Robust parametric and semi-parametric spot fitting for spot array images.* In *International Conference on Intelligent Systems for Molecular Biology; ISMB*, volume 8, pp. 46–56. Vienna University of Technology, Pattern Recognition and Image Processing Group, AAAI Press (2000).

[55] M. D. Abramoff, P. J. Magelhaes, and S. J. Ram. *Image Processing with ImageJ.* Biophotonics International **11**, 36–42 (2004).

[56] W. S. Rasband. *ImageJ* (1997-2009). `http://rsb.info.nih.gov/ij/`. U. S. National Institutes of Health, Bethesda, Maryland, USA.

[57] S. Kimball, P. Mattis, and The GIMP Development Team. *GIMP - GNU Image Manipulation Program* (September, 30th 2009). `http://www.gimp.org/`.

[58] E. C. Friedberg, G. C. Walker, and W. Siede. *DNA repair and mutagenesis.* Second edition. American Society for Microbiology (1995).

[59] B. Van Houten, D. L. Croteau, M. J. DellaVecchia, H. Wang, and C. Kisker. *'Close-fitting sleeves': DNA damage recognition by the UvrABC nuclease system.* Mutation Research **577**, 92–117 (2005).

[60] D. Bootsma, G. Weeda, W. Vermeulen, H. V. Vuuren, C. Troelstra, P. V. D. Spek, and J. Hoeijmakers. *Nucleotide Excision Repair Syndromes: Molecular Basis and Clinical Symptoms.* Philosophical Transactions of the Royal Society of London. Series B: Biological Sciences **347**, 75–81 (1995).

[61] R. J. Bienstock, M. Skorvaga, B. S. Mandavilli, and B. Van Houten. *Structural and Functional Characterization of the Human DNA Repair Helicase XPD by Comparative Molecular Modeling and Site-directed Mutagenesis of the Bacterial Repair Protein UvrB.* Journal of Biological Chemistry **278**, 5309–5316 (2003).

[62] J. J. Truglio, D. L. Croteau, B. Van Houten, and C. Kisker. *Prokaryotic Nucleotide Excision Repair: The UvrABC System.* Chemical Reviews **106**, 233–252 (2006).

[63] K. Theis, M. Skorvaga, M. Machius, N. Nakagawa, B. Van Houten, and C. Kisker. *The nucleotide excision repair protein UvrB, a helicase-like enzyme with a catch.* Mutation Research/DNA Repair **460**, 277–300 (2000).

[64] J. J. Truglio, E. Karakas, B. Rhau, H. Wang, M. J. DellaVecchia, B. Van Houten, and C. Kisker. *Structural basis for DNA recognition and processing by UvrB.* Nature Structural & Molecular Biology **13**, 360–364 (2006).

[65] K. El Kirat, I. Burton, V. Dupres, and Y. F. Dufrene. *Sample preparation procedures for biological atomic force microscopy.* Journal of Microscopy **218**, 199–207 (2005).

[66] K. Yoshida, M. Yoshimoto, K. Sasaki, T. Ohnishi, T. Ushiki, J. Hitomi, S. Yamamoto, and M. Sigeno. *Fabrication of a New Substrate for Atomic Force Microscopic Observation of DNA Molecules from an Ultrasmooth Sapphire Plate.* Biophysical Journal **74**, 1654–1657 (1998).

[67] Mineral database (mindat.org). *Illite datasheet.* `http://www.mindat.org/min-2011.html`.

[68] G. Schitter. *Advanced Mechanical Design and Control Methods for Atomic Force Microscopy in Real-Time.* In *Proceedings of the 2007 American Control Conference*, pp. 3503–3508 (2007).

[69] D. Sadava, H. C. Heller, G. H. Orians, W. K. Purves, and D. M. Hillis. *Life: the science of biology.* 8th edition. Sinauer Associates, Inc. (2008).

A. Appendix

A.1. Symbols

In equations, Roman letters are used for variables related to the topography/AFM images, while Greek letters denote optical quantities. s_X denotes the error and $\bar{X}$ the mean of X, respectively. Symbols with many instances are indexed (X_i) and their number is referred to as N_X. For optical coordinates, a star $(\star)$ indicates coordinates that have been transformed. The following list contains the symbols used throughout this document. All symbols not listed here are explained in their immediate context and only effective there.

$\bar{d}$ Mean distance of fiducial markers after the transformation

$\hat{m}$ Transformation matrix

N (without index) photon count

N_F number of fiducial markers used for the transformation

N_R number of the regions containing a fluorescent signal to be fitted

λ Wavelength (light)

r_A, r_O Nominal (pixel) resolution of the AFM and optical image, respectively

ϱ Roughness (of an AFM image or substrate) evaluated according to Eq. (1)

s_A Mean error of the AFM positions, generally taken to be $r_A/2$

s_O Mean error off the optical positions

s_R Total error/accuracy of the registration, evaluated according to Eq. (19)

SNR Signal to noise ratio, evaluated according to Eq. (6)

$\vec{t}$ Transformation offset

x, y, z AFM coordinates (nm).

ξ, υ, ζ Coordinates in the optical images (pixels / photon counts)

A.2. Buffers

Composition of the buffers used:

Binding buffer 50 mM Tris, 50 mM KCl, 10 mM MgCl$_2$, 5.0 mM DTT,

10 mM ATP (pH 7.5)

Deposition buffer 25 mM HEPES, 25 mM Na-Acetate and 10 mM Mg-Acetate (pH 7.5).

QD-Storage buffer 90 mM Tris, 90 mM Borate, 1.66 mM EDTA (pH 7.8)

All buffers were filtered through 20 nm pores after preparation and stored at −20°C.

A.3. Image processing code

The entire image processing and registration code used for this work was written using *Mathematica 6* in notebook mode.

The code found below is not optimized for readability but left as used for the above analyses. Some parts of the code can be switched on and off for special purposes, e.g. for quickly obtaining information about the optical image only, or processing many images using the same fiducial markers. Apart from these small changes, the code is executed as-is, cell per cell from top to bottom.

The code is printed for reference purposes and not further commented on (except for the inline comments), since all of its physically relevant functions are discussed in the main text.

AFM/FIONA Registration (c) David v0.7.1

```
(******************************************************************************************)
(* All variables starting with T denote properties of the Target (=reference) image, the ones  *)
(*  starting with P of the Projection (=template) image                                         *)
(******************************************************************************************)
(* Basic initialization *)
CollectedResults={{"# Collected Results"},{"# "}};
CollectedCoordinates={{"# Collected Coordinates","","",""},{"#", "x", "y", "dxy"}};
FileNumber=0;
(* Only works in graphical environment, path=relative to Notebook (.nb) file *)
SetDirectory[NotebookDirectory[]];


(*** Definition of basic functions: ***)


(* Conversion of gray value to photon counts *)
(* Photon count = (Pixel gray value - offset) * Gain conversion factor / EM Gain / Analog Gain *)
PhotonCounts[PixelValue_]:= Round[(PixelValue-CameraOffset)* GCF / EMGain / AnalogGain];


(* Define Fit function *)
Gauss2D[x_,y_,mx_,my_,std_,zmax_,zoff_]=zmax*Exp[-0.5/std^2*((x-mx)^2+(y-my)^2)]+zoff;


(* Error Calculation for Gauss Fitting: Er1=background, Er2=photon noise, Er3=rasterization *)
(* backgournd conversion? !!! *)
(* Evaluation scale invariant in x,y => evaluation in pixel units possilbe *)
(* n = number of photons; s = standard deviation of gaussian fit; a = camera pixel size; b =
background noise *)
Er1[N_,s_,a_,b_]:=s^2*b/a/N*Sqrt[8 Pi];
Er2[N_,s_]:=s/Sqrt[N];
Er3[N_,a_]:=a/Sqrt[12 N];
FIONAError[N_,s_,a_,b_]:=Sqrt[Er1[N,s,a,b]^2+Er2[N,s]^2+ Er3[N,a]^2];


(* Selection Rectangles = Box of size s @ (x,y) *)
SelectionRectangles[XYS_,Ymax_]:=Table[Graphics[{EdgeForm[Red],FaceForm[],Rectangle[{XYS[[Mnr,1]],Y
max-XYS[[Mnr,2]]},{XYS[[Mnr,1]]+XYS[[Mnr,3]]},Ymax-
(XYS[[Mnr,2]]+XYS[[Mnr,3]])}]],Text[Mnr,{XYS[[Mnr,1]],Ymax-XYS[[Mnr,2]]},Background->Red,FormatType-
>StandardForm]}],{Mnr,Length[XYS]}];
SelectionRectangles[XYS_,Ymax_,SText_,SColor_]:=Table[Graphics[{EdgeForm[SColor],FaceForm[],Rectang
le[{XYS[[Mnr,1]],Ymax-XYS[[Mnr,2]]},{XYS[[Mnr,1]]+XYS[[Mnr,3]]},Ymax-
(XYS[[Mnr,2]]+XYS[[Mnr,3]])}]],Text[SText[[Mnr]],{XYS[[Mnr,1]],Ymax-XYS[[Mnr,2]]},Background-
>SColor,FormatType->StandardForm]}],{Mnr,Length[XYS]}];
(* FitIndicators = HairCrosses @ Coordinates *)
FitIndicators[Coords_,Ymax_]:=Table[Graphics[{Blue,Line[{{Coords[[Mnr,1]]-10,Ymax-
Coords[[Mnr,2]]},{Coords[[Mnr,1]]+10,Ymax-Coords[[Mnr,2]]}}],Line[{{Coords[[Mnr,1]],Ymax-
Coords[[Mnr,2]]-10},{Coords[[Mnr,1]],Ymax-Coords[[Mnr,2]]+10}}]}],{Mnr,Length[Coords]}];
FrontEndExecute[FrontEndToken["EvaluateNextCell"]];FrontEndExecute[FrontEndToken["EvaluateNextCell"
]];


(* All sorts of flags *)
SuperFastAnalysis=False;
StopNumber=20;
AutomaticAnalysis=False;
OverlayGeneration=False;
ProbabilityMapGeneration=True;
ShowMany3DPlots=False;
UseTracker={1,2}; (* AFM: 1=Max., 2=Center(!); FIONA: 1=Gauß, with constraints, 2=Gauß,3=Center *)
FrontEndExecute[FrontEndToken["EvaluateNextCell"]];FrontEndExecute[FrontEndToken["EvaluateNextCell"
]];
```

Initialization/Globals

```
(* Start *)
DefaultMarkerSize=12;
BadPoints={};


(* Background Marker *)
BMarker={1,200,DefaultMarkerSize};


(* In nm/pixel *)
TResolution=7.8125;
PResolution=62.5;


(* Import Image settings *)
If[SuperFastAnalysis,AutomaticAnalysis=True;FileNumber++, FileNumber=1];
FileNameBase="df090726_QDgl_";
FileNameBase=FileNameBase<>IntegerString[FileNumber,10,3];
TFile = FileNameBase<>"T.tif";
PFile=FileNameBase<>"P.tif";
IFile=FileNameBase<>"I.txt";
OFile=FileNameBase<>"P-Overlay.tif";
ProbFile=FileNameBase<>"Probability.tif";
DOFile=FileNameBase<>".results.txt";
If[AutomaticAnalysis,
  <<(IFile),
  TFile="df090726_QDgl_0003_HtT.tif";
  PFile="df090725_QDgl_0002e_projected_ROI_CCD4x.tif";
  ];
```

```
(* Print excerpt of comment for reading Gain values *)
If[AutomaticAnalysis,,
  PComment=Import[PFile,"Comments"];
  Print[StringTake[PComment,Transpose[{StringPosition[PComment,"c_Gain"|"c_SensorGain1"][[All,1]],
  StringPosition[PComment,Shortest[("c_Gain"|"c_SensorGain1")~~__~~"\n"]][[All,2]]}]]]
  EMGainRelative=190;
  ];
(* In case something a file is not available or unsuitable, set this anyway *)
PImageMax=Check[2^Import[PFile,"BitDepth"] - 1,1];
TImageMax=Check[2^Import[TFile,"BitDepth"] - 1,1];

(* Standard Camera settings *)
CameraOffset=1; (* should be determined by taking a 'dark' picture, but neglectable, see Tech Note
*)
EMGainMax=1000; (* +-200 *)(* 1200 neu, verringert sich im Laufe des Kameralebens, geschätzt *)
FullWellCapacity=370000; (* from manual *)
(* Gain conversion factor;Berechnung nach Mr. Herrmann von Hamamatsu *)
EMGain=EMGainRelative/255 * EMGainMax;
GCF=FullWellCapacity/(PImageMax - CameraOffset);
AnalogGain=5;

(* Basic test for existing input files *)
Catch[
  If[FileType[TFile]!=File,Throw["File >"<>TFile<>"< not found!"]];
  If[FileType[PFile]!=File,Throw["File >"<>PFile <>"< not found!"]];
  Print["Ok."];
  If[AutomaticAnalysis, FrontEndExecute[
  FrontEndToken["EvaluateNextCell"]];FrontEndExecute[FrontEndToken["EvaluateNextCell"]];];
  ];

 Ok.
```

Image Analysis, AFM

```
(* Import file; That way 1. Coordinate=x, 2nd coordinate=y, both ascending from top left in image
*)
(* By importing GrayLevels, the values will be automatically normalized to the interval [0:1] *)
TImageData =Transpose[Import[TFile,"GrayLevels"]];
(* Marker Definition *)
(* Target Markers(x,y,size) *)
If[AutomaticAnalysis,
  TMarkers=Array[Clip[Round[TMarkers[[#1,#2]]],{1,Dimensions[TImageData][[1]]-
DefaultMarkerSize}]&,Dimensions[TMarkers]];,
  (* Insert Markers by hand here : *)
  TMarkers=Round[{{18,95,20},{125,32,20},{215,98,20},{325,62,20},{214,407,20}}];
  ];
(* Fill in DefaultMarkerSize where necessary *)
TMarkers=Array[If[Length[TMarkers[[#]]]0 3,TMarkers[[#]],Append[TMarkers[[#,1;;2]],DefaultMarkerSiz
e]]&,Length[TMarkers]];
(* Delete Bad Markers *)
TMarkers=Delete[TMarkers,Partition[BadPoints,1]];
(* Select Areas *)
TFitArea = Table[TImageData[[TMarkers[[Mnr,1]]+1;;TMarkers[[Mnr,1]]+TMarkers[[Mnr,3]],
  TMarkers[[Mnr,2]]+1;;TMarkers[[Mnr,2]]+TMarkers[[Mnr,3]]]],{Mnr,Length[TMarkers]}];
(* Initialize set of fit parameters *)
TLocalFitParams=ConstantArray[0,{Length[TMarkers],3}];

(* Find Max *)
(* The middle one of equally high points is selected without thinking!!! Not perfectly nice. *)
(* TODO: Implement Center of Mass tracker !!! (not so important, now) *)
If[UseTracker[[1]]==1,
  HighestPoints=Array[(Position[TFitArea[[#]],Max[TFitArea[[#]]]])&,Length[TMarkers]];

TLocalFitParams=Array[(HighestPoints[[#,Ceiling[Length[HighestPoints[[#]]]/2]]])&,Length[TMarkers]]
;
  ];
TFitParams=TLocalFitParams [[All,1;;2]]+TMarkers[[All,1;;2]];

(* Show Data & Image (for verification) *)
(* Print["Local fit parameters: ",(Prepend[LocalFitParams,{"x","y"}]//MatrixForm)]; *)
If[AutomaticAnalysis,,
  (* Selection Rectangles *)
  TSelections=SelectionRectangles[TMarkers,Dimensions[TImageData][[1]]];
  AppendTo[TSelections,Graphics[Text["0-Gx->",{Dimensions[TImageData][[1]]/2,0},Background->Red]]];
  AppendTo[TSelections,Graphics[Text["^Gy",{0,Dimensions[TImageData][[1]]/2},Background->Red]]];
  TFitIndicators=FitIndicators[TFitParams,Dimensions[TImageData][[2]]];
  Print[Show[Graphics[Raster[Reverse@Transpose[TImageData]]],TSelections,TFitIndicators] ];
  ];
(* Data for import in Affine Transformation *)
(* List of (x,y,statistical weight=1/area), possible area here =~ PixelSize *)
(* -0.5 pixels to place marker in the center of the pixel!!! *)
TPoints=Table[{TFitParams[[Mnr,1]]-0.5,TFitParams[[Mnr,2]]-0.5,2},{Mnr,Length[TMarkers]}];
(* Jump to next section in automatic mode *)
If[AutomaticAnalysis,
  Print["Ok."];,
  Print["Target Points: ",Prepend[TPoints,{"x","y","weight"}]//MatrixForm];
  ];
If[AutomaticAnalysis,

FrontEndExecute[FrontEndToken["EvaluateNextCell"]];FrontEndExecute[FrontEndToken["EvaluateNextCell"
]];];
```

```
Target Points:  ( {{x, y, weight},
                   {27.5, 104.5, 2},
                   {137.5, 40.5, 2},
                   {227.5, 106.5, 2},
                   {333.5, 73.5, 2},
                   {227.5, 418.5, 2}  } )
```
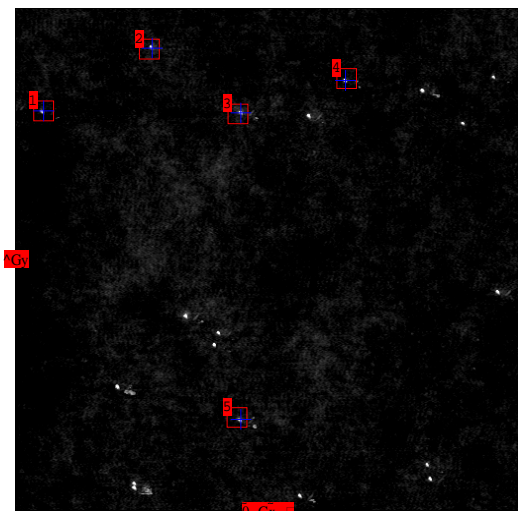
Image Analysis, FIONA

```
(* Import file; That way 1. Coordinate=x, 2. coordinate=y, both ascending from top left in image *)
(* By importing GrayLevels, the values will be automatically normalized to the interval [0:1] *)
PImageData = Transpose[Import[PFile,"GrayLevels"]];
(* Marker Definition *)
(* Projection Markers(x,y,size) *)
If[AutomaticAnalysis,
  PMarkers=Array[Clip[Round[PMarkers[[#1,#2]]],{1,512-DefaultMarkerSize}]&,Dimensions[PMarkers]];,
  (* Insert Markers by hand here : *)
  PMarkers=Round[{{83,165},{95,159},{105,165},{118,161},{104,200}}];
  ];
(* Fill in DefaultMarkerSize where necessary *)
PMarkers=Array[If[Length[PMarkers[[#]]]❶3,PMarkers[[#]],Append[PMarkers[[#,1;;2]],DefaultMarkerSiz
e]]&,Length[PMarkers]];
(* Delete Bad Markers *)
PMarkers=Delete[PMarkers,Partition[BadPoints,1]];
(* Calculate Background (in image brightness units from green marker region) *)
RawBG=N[PImageMax
*Mean[Flatten[PImageData[[BMarker[[1]]+1;;BMarker[[1]]+BMarker[[3]],BMarker[[2]]+1;;BMarker[[2]]+BM
arker[[3]]]]]]];
BGPhotons=Round[PhotonCounts[RawBG]];
(* Select Areas *)
PFitArea = Table[PImageData[[PMarkers[[Mnr,1]]+1;;PMarkers[[Mnr,1]]+PMarkers[[Mnr,3]],
  PMarkers[[Mnr,2]]+1;;PMarkers[[Mnr,2]]+PMarkers[[Mnr,3]]]],{Mnr,Length[PMarkers]}];
(*Print["Selected Areas:
",(Table[Dimensions[PFitArea[[Mnr]]],{Mnr,Length[PMarkers]}]//MatrixForm)];*)
(* Transform for FindFit *)
PFFData =Table[Flatten[
Table[{xi,yi,PFitArea[[Mnr,xi,yi]]},{xi,PMarkers[[Mnr,3]]},{yi,PMarkers[[Mnr,3]]}],1],
  {Mnr,Length[PMarkers]}];

(* Initialize set of fit parameters: (mx,my,std,zmax,zoff) *)
PLocalFitParams=ConstantArray[0,{Length[PMarkers],5}];
PFitParams=ConstantArray[0,{Length[PMarkers],5}];

(* Do Fits, perhaps choose sensible starting values by hand *)
(* TODO: Choosing anything by hand is bad: 15 =max. Gauß-width is chosen haphazardly!!! *)
(* Long term aim: Automatisieren mit zweistufigem Fitting-Verfahren *)
 For[Mcount=1,Mcount<=Length[PMarkers],Mcount++,
  Switch[UseTracker[[2]],
  1,PLocalFitParams[[Mcount]]={mx,my,std,zmax,zoff}/.FindFit[PFFData[[Mcount]],
   {Gauss2D[x,y,mx,my,std,zmax,zoff],{0<=mx<=Dimensions[PImageData][[1]],
   0<=my<=Dimensions[PImageData][[2]],std>0}},{{mx,PMarkers[[Mcount,3]]/2},
   {my,PMarkers[[Mcount,3]]/2},{std,3},{zmax,1},{zoff,0}},{x,y}];,
  2,PLocalFitParams[[Mcount]]={mx,my,std,zmax,zoff}/.FindFit[PFFData[[Mcount]],
   {Gauss2D[x,y,mx,my,std,zmax,zoff],std>0},{{mx,PMarkers[[Mcount,3]]/2},
   {my,PMarkers[[Mcount,3]]/2}, {std,3},{zmax,1},{zoff,0}},{x,y}];,
  3,PLocalFitParams[[Mcount]]=N[{Sum[RowNr*Total[PFitArea[[Mcount,RowNr,All]]-RawBG/PImageMax],
   {RowNr, Length[PFitArea[[Mcount,All,1]]]}]/Sum[Total[PFitArea[[Mcount,RowNr,All]]-
   RawBG/PImageMax],{RowNr, Length[PFitArea[[Mcount,All,1]]]}],  Sum[ColNr*
   Total[PFitArea[[Mcount,All,ColNr]]-RawBG/PImageMax],{ColNr, Length[PFitArea[[Mcount,1]]]}] /
   / Sum[Total[PFitArea[[Mcount,All,ColNr]]-RawBG/PImageMax],
   {ColNr,Length[PFitArea[[Mcount,1]]]}], PMarkers[[Mcount,3]]/2,1,1}];
  ];
(* Correct x- and y-offset *)
PFitParams[[All,1;;2]]=PLocalFitParams [[All,1;;2]]+PMarkers[[All,1;;2]];
PFitParams[[All,3;;5]]=PLocalFitParams [[All,3;;5]];

(* Show Data and Image (for verification) *)
(* Print["Local fit parameters: ,(Prepend[PLocalFitParams,{"x","y","std","zmax","zoff"}])]; *)
(* Print["Found the following fit parameters: ",
  (Prepend[PFitParams,{"x","y","std","zmax","zoff"}]//MatrixForm)]; *)
```

```
PSelections=SelectionRectangles[PMarkers,Dimensions[PImageData][[2]]];
If[True,AppendTo[PSelections,SelectionRectangles[{BMarker},Dimensions[PImageData][[2]],{"B"},Green]
]];
AppendTo[PSelections,Graphics[Text["0-Gx->",{Dimensions[PImageData][[1]]/2,0},Background->Red]]];
AppendTo[PSelections,Graphics[Text["^Gy",{0,Dimensions[PImageData][[2]]/2},Background->Red]]];
PFitIndicators=FitIndicators[PFitParams,Dimensions[PImageData][[2]]];
If[SuperFastAnalysis,,
  Print[Show[Graphics[Raster[Reverse@Transpose[PImageData]]],PSelections,PFitIndicators]] ];


(* Show fits as 3D plots (for verification) *)
If[ShowMany3DPlots, DataPlots=Table[ListPlot3D[Transpose[PFitArea[[Mnr]]],
  PlotRange->Full,ColorFunction->Function[{xy,yv,zv},Hue[0.58,zv+0.33,1]],
  PlotStyle->Opacity[0.5],Mesh->None],{Mnr,Length[PMarkers]}];
  FitPlots=Table[Plot3D[Gauss2D[xg,yg,PLocalFitParams[[Mnr,1]],PLocalFitParams[[Mnr,2]],
  PLocalFitParams[[Mnr,3]],PLocalFitParams[[Mnr,4]],PLocalFitParams[[Mnr,5]]],
  {xg,1,PMarkers[[Mnr,3]]},{yg,1,PMarkers[[Mnr,3]]},ColorFunction->Function[{xy,yv,zv},
  Hue[0.1,zv+0.33,1]],PlotStyle->Opacity[0.5],Mesh->None,PlotRange->{0,1}],{Mnr,Length[PMarkers]}];
  Print[Table[{Mnr,Show[FitPlots[[Mnr]],DataPlots[[Mnr]],PlotRange->{0,1},
  ViewPoint->{0,-1,1.5}]},{Mnr,Length[PMarkers]}]];
  ];


(*** Error Calculation ***)
(*Pixel units are not converted into nm here, but grayscale values are converted into photon
counts!*)
(* Total Photons (per peak) *)
(* Include only counts within 2 standard deviations *)
Np[Mnr_]:=Total[PhotonCounts[PImageMax*Flatten[  Array[If[Sqrt[(#1-PLocalFitParams[[Mnr,1]])^2+
  (#2-PLocalFitParams[[Mnr,2]])^2]<PFitParams[[Mnr,3]]*2,Max[PFitArea[[Mnr,#1,#2]],0],0]&,
  Dimensions[PFitArea[[Mnr]]] ]]]];

PFitErrors=Table[{Mnr,Np[Mnr],FIONAError[Np[Mnr],PFitParams[[Mnr,3]],1,BGPhotons],Er1[Np[Mnr],
  PFitParams[[Mnr,3]],1,BGPhotons],Er2[Np[Mnr],PFitParams[[Mnr,3]]],Er3[Np[Mnr],1],
  Pi*PFitParams[[Mnr,3]]^2*BGPhotons},{Mnr,Length[PMarkers]}];

(* Data for import in Affine Transformation *)
(* List of (x,y,statistical weight) *)
PPoints=Table[{PFitParams[[Mnr,1]],PFitParams[[Mnr,2]],1/PFitErrors[[Mnr]][[3]]},
  {Mnr,Length[PMarkers]}];

(* Collect resulting coordinates in global variable *)
If[MemberQ[CollectedCoordinates[[All,1]],FileNumber],
  CollectedCoordinates[[ Flatten[Position[CollectedCoordinates[[All,1]],FileNumber] ]
]]={FileNumber,PPoints},
  AppendTo[CollectedCoordinates,{FileNumber,PPoints}] ];

(* TODO: Add S/N to error information!! *)
Print["Projection Points: ",Prepend[PPoints,{"x","y","weight"}]//MatrixForm,",
  Background (counts|photons): ",Round[RawBG],"|",BGPhotons];
If[AutomaticAnalysis,,
  Print["Error Information: ,Prepend[N[Transpose[Transpose[PFitErrors]*
  {1,1,PResolution,PResolution,PResolution,PResolution,1,1}]],{"#","Photons (incl. bg)",
  "Total Error / nm","background error / nm","Gauss error / nm","raster error / nm",
  "background photons","Peak Height (Photons)"}]//MatrixForm];
  ];
If[SuperFastAnalysis,FrontEndExecute[FrontEndToken["EvaluateNextCell"]];
  FrontEndExecute[FrontEndToken["EvaluateNextCell"]];];
```
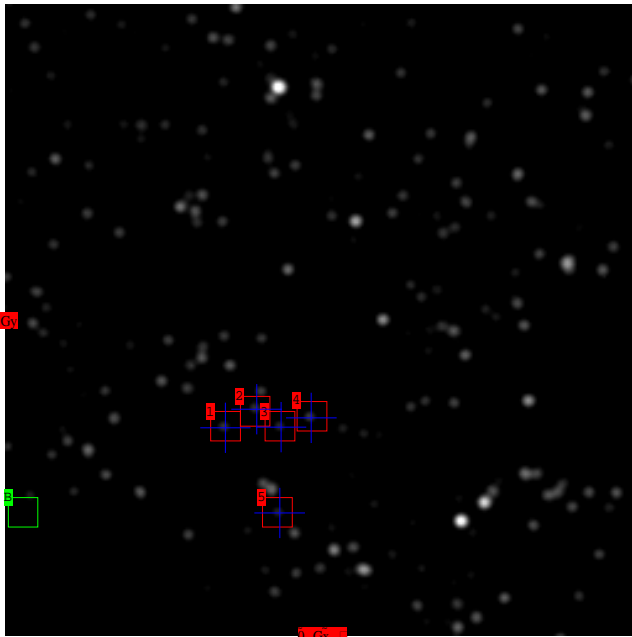


```
 Projection Points:  ( { {x, y, weight},
                        {88.9992, 171.626, 11.1092},
                        {101.592, 164.114, 10.7267},
                        {111.491, 171.426, 9.71966},
                        {123.706, 167.67, 11.8869},
                        {110.927, 206.278, 9.15289} } ) , Background (counts|photons): 0.1667 | 0
Error Information:  ( {  {#, Photons (incl. bg), Total Error / nm, background error / nm, Gauss
```

```
              error / nm, raster error / nm, background photons},
                              {1., 202., 5.62594, 0., 5.48085, 1.26944, 0.},
                              {2., 189., 5.82656, 0., 5.67684, 1.31238, 0.},
                              {3., 133., 6.43026, 0., 6.23705, 1.56446, 0.},
                              {4., 231., 5.25789, 0., 5.12213, 1.18709, 0.},
                              {5., 124., 6.82844, 0., 6.63343, 1.62024, 0.}  } )
```

Transformation Calculation

```
ErrorSumsList=Sum[({{a1,a2},{a3,a4}}.TPoints[[i,1;;2]]+{b1,b2} - PPoints[[i,1;;2]])^2,
  {i,Length[PPoints]}];
WeightedErrorSumsList=Sum[({{a1,a2},{a3,a4}}.TPoints[[i,1;;2]]+{b1,b2}-PPoints[[i,1;;2]])^2 *
  PPoints[[i,3]]^2*TPoints[[i,3]]^2,{i,Length[PPoints]}];

(* Vectorial addition of x and y component. Compared to direct sum, only the
  Minimum value differs, while the coefficients stay the same! *)
ErrorSum=RootMeanSquare[ErrorSumsList];
WeightedErrorSum=RootMeanSquare[WeightedErrorSumsList];

(* If WeightedErrorSum (instead of ErrorSum) is minimized, the uncertainty of each point is taken
into    accout *)
NMinimize[WeightedErrorSum,{a1,a2,a3,a4,b1,b2}];
CoefficientsRule=%[[2]];
(* Important: WeightedErrorSum is for minimizing only. The true absolute value of the mean *)
(* deviation is given by ErrorSum itself: *)
TransformationError=ErrorSum/.CoefficientsRule;
TransformationM={{a1,a2},{a3,a4}}/.CoefficientsRule;
TransformationO={b1,b2}/.CoefficientsRule;

(* Error Calculation *)
(* Rough estimation, in nm *)
(* The full error is computed externally using the precision information from many images *)
FullError=Sqrt[(Mean[TResolution/TPoints[[All,3]]])^2+(Mean[PResolution/PPoints[[All,3]]])^2;
(* Mean distance *)
MeanDistance=Norm[Sum[Abs[TransformationM.TPoints[[i,1;;2]]+TransformationO-PPoints[[i,1;;2]]],
  {i,Length[PPoints]}]/Length[PPoints]];

(* Target or Projection Resolution limiting??? *)
If[AutomaticAnalysis,,
  Print["Transformation calculated:"
,(TransformationM//MatrixForm),({"x","y"}//MatrixForm),"+",(TransformationO//MatrixForm), ";"];
  Print["Error from Transformation: " ,TransformationError/Length[PMarkers]*TResolution," nm"];
  Print["Error from AFM tracking: " ,Mean[TResolution/TPoints[[All,3]]]," nm"];
  Print["Error from FIONA tracking: " ,Mean[PResolution/PPoints[[All,3]]]," nm"];
  Print["Mean distance of matching points: (" ,MeanDistance*TResolution,"+-",FullError,") nm"];
  ];
Print["Ok."];
If[AutomaticAnalysis,
  FrontEndExecute[FrontEndToken["EvaluateNextCell"]];
  FrontEndExecute[FrontEndToken["EvaluateNextCell"]];];
 Transformation calculated:
                   ( { {0.113117, -0.00221434},
                       {-0.00153175, 0.111667}} ) *
                   ( { {x}, {y} } ) +
                   ( { {85.1059},  {158.916} } ) ;
 Error from Transformation:  0.0320583  nm
 Error from AFM tracking:  3.90625  nm
 Error from FIONA tracking:  5.99382  nm
 Mean distance of matching points: ( 0.576781 +- 7.15435 ) nm
 Ok.
(* Possibility to compare with the true values (for simulated data) *)
(* Or enter by hand here: *)
If[AutomaticAnalysis,,
  TruePoints={{1,1},{2,2}};
  TruePPoints={{1,1},{2,2}};
  TrueTransM={{1,0},{0,1}};
  TrueTransO={1,1};
  ];
TruePoints=Delete[TruePoints,Partition[BadPoints,1]];
TruePPoints=Delete[TruePPoints,Partition[BadPoints,1]];
If[AutomaticAnalysis,,
  Print["Transformation Deviation (%): ",(Abs[(TransformationM-TrueTransM)/TrueTransM]*100
  //MatrixForm),",",(Abs[(TransformationO-TrueTransO)/TrueTransO]*100//MatrixForm), ";"];
  Print["Mean Positional Deviation (overall): ",Norm[Sum[Abs[TrueTransM.TruePoints[[i,1;;2]]+
  TrueTransO-PPoints[[i,1;;2]]],{i,Length[PPoints]}]/Length[PPoints]]*TResolution, " nm"];
  Print["Mean FIONA mismatch: ",Norm[Sum[Abs[PFitParams[[All,1;;2]]-TruePPoints],
  {i,Length[PFitParams]}]]," nm"];
  ];
Print["Ok."];
If[AutomaticAnalysis, FrontEndExecute[FrontEndToken["EvaluateNextCell"]];
  FrontEndExecute[FrontEndToken["EvaluateNextCell"]];];
 Ok.
(* Output of info file *)
Inf=Flatten[{FileNumber,
  Length[TMarkers],
  RawBG,
  TransformationError/Length[PMarkers]*TResolution,
  Mean[1/TPoints[[All,3]]]*TResolution,
  Mean[1/PPoints[[All,3]]]*PResolution,
  MeanDistance*TResolution,
  FullError,Norm[Sum[Abs[TrueTransM.TruePoints[[i,1;;2]]+TrueTransO-PPoints[[i,1;;2]]],
    {i,Length[PPoints]}]/Length[PPoints]]*TResolution,
  Norm[Sum[Abs[TruePPoints[[i,1;;2]]-PPoints[[i,1;;2]]],
    {i,Length[PPoints]}]/Length[PPoints]]*PResolution,"",
  N[Mean[N[Transpose[Transpose[PFitErrors] *
    {0,1,PResolution,PResolution,PResolution,1,1}]]]]}];
InfoFile=OpenWrite[DOFile];
WriteString[InfoFile,"(* Info for File: ",FileNameBase," *)\n","Number of tracked Peaks:
```

```
          ",Inf[[2]],"\n","Transformation calculated: " ,TransformationM,"{x,y}","+",TransformationO,
          ";\n","Raw Background Noise: ",Inf[[3]],"\n","Error from Transformation: ",Inf[[4]],"
          nm\n","Error from AFM tracking: " ,Inf[[5]]," nm\n","Error from FIONA tracking: " ,Inf[[6]],"
          nm\n","Sub-Errors from FIONA tracking (#photons,full,bg,ps,pix): " ,Inf[[12;;16]]," in
          {#,nm,nm,nm}\n","Mean distance of matching points: (" ,Inf[[7]],"+-",Inf[[8]],")
          nm\n","Transformation Deviation (%): ",AccountingForm[Abs[(TransformationM-
          TrueTransM)/TrueTransM]*100],",",AccountingForm[Abs[(TransformationO-
          TrueTransO)/TrueTransO]*100], "\n","Mean Positional Deviation: ",Inf[[9]], " nm\n","Spreadsheet
          line follows:\n",StringReplace[ToString[Inf],{"{"|"}"->"",", "->"\t"}],"\n"];
  Close[InfoFile];
  If[MemberQ[CollectedResults[[All,1]],Inf[[1]]],
    CollectedResults[[ Flatten[Position[CollectedResults[[All,1]],Inf[[1]] ] ] ]]=Inf,
    AppendTo[CollectedResults,Inf]];
  Clear[Inf];
  Print["Ok."];
  If[AutomaticAnalysis,
    FrontEndExecute[FrontEndToken["EvaluateNextCell"]];
    FrontEndExecute[FrontEndToken["EvaluateNextCell"]];];
   Ok.
```

Resampling / Image Generation

```
(* Resample within the image boundaries. Outside=0 *)
InverseM=Inverse[TransformationM];
If[OverlayGeneration,
  OverlayData=Array[(If[x>0 && x<Dimensions[PImageData][[1]]&&y>0&&y<Dimensions[PImageData][[2]],
    Floor[PImageData[[x,y]]*PImageMax],0]/.{x->Round[TransformationM.{#1,#2}+TransformationO][[1]],
    y->Round[TransformationM.({#1,#2})+TransformationO][[2]]})&,Dimensions[TImageData]];
  (* Export to file *)
  Export[OFile,"Data"->Transpose[OverlayData],"Rules",ImageSize->Dimensions[TImageData],
    "ColorSpace"->"GrayLevel","ImageEncoding"->"LZW","BitDepth"->Round[Log[2,PImageMax]]];
  Print["Fluorescence Overlay: Ok."]; ];
(* Probability-Map *)
(* Draw standard deviation around each point *)
(* Broadened PBroaden times (else hardly visible, s. confined to very few (or even less than 1) px)
*)
If[ProbabilityMapGeneration,
  PBroaden=1;
  ProbabilityData=ConstantArray[0,Dimensions[TImageData]];
  For[Pnr=1,Pnr<=Length[PPoints],Pnr++, {ProbX,ProbY}=InverseM.(PPoints[[Pnr,1;;2]]-
TransformationO);
  ProbabilityData=ProbabilityData+Array[(
  If[(#1-ProbX)^2+(#2-ProbY)^2<(PBroaden*2*PResolution/TResolution/PPoints[[Pnr,3]])^2,

Ceiling[Gauss2D[#1,#2,ProbX,ProbY,PBroaden*PResolution/TResolution/PPoints[[Pnr,3]],254,0]],0])&,
      Dimensions[TImageData]];];
  Export[ProbFile,"Data"->Transpose[ProbabilityData],"Rules",ImageSize->Dimensions[TImageData],
    "ColorSpace"->"GrayLevel","ImageEncoding"->"LZW","BitDepth"->8];
  Print["Probability Map: Ok."];
  ];
If[SuperFastAnalysis && FileNumber<StopNumber,NotebookFind[EvaluationNotebook[],
  "(* Start *)"] FrontEndExecute[FrontEndToken["EvaluateNextCell"]];];
 Ok.
```

Cross-Sections

```
(* Show both 2D sections and fits (for verification): "Ingrid's Plot" *)
(* Still some error? Should TPoints instead of TMarkers be used?!? *)
PixelCenter=PC=-0.5*PResolution/TResolution;
(* Is rescaling necessary? à la NxTr[Matrx]/2 *)
AFMSections=Table[ListLinePlot[TFitArea[[Mnr,Round[TPoints[[Mnr,1]]-TMarkers[[Mnr,1]]],All]],
  DataRange->{(TMarkers[[Mnr,2]]+PC)*TResolution,(TMarkers[[Mnr,2]]+TMarkers[[Mnr,3]]+PC) *
  TResolution},InterpolationOrder->0,PlotStyle->Directive[Hue[Mnr/Length[TMarkers]],Dotted],
  PlotRange->{0,1.1},AspectRatio->0.2,ImageSize->{500}],{Mnr,Length[TMarkers]}];
FIONASections=Table[ListLinePlot[PFitArea[[Mnr,Round[PPoints[[Mnr,1]]]-PMarkers[[Mnr,1]]],All]],
  DataRange->{(PMarkers[[Mnr,2]])*PResolution,(PMarkers[[Mnr,2]]+PMarkers[[Mnr,3]])*PResolution},
  InterpolationOrder->0,PlotRange->All,AspectRatio->0.2,ImageSize->{400}],{Mnr,Length[TMarkers]}];
FIONATrack=Table[Plot[Gauss2D[yg,PPoints[[Mnr,2]]*PResolution,
  (PMarkers[[Mnr,2]]+PLocalFitParams[[Mnr,2]])*PResolution,PPoints[[Mnr,2]]*PResolution,
  PLocalFitParams[[Mnr,3]]*PResolution,PLocalFitParams[[Mnr,4]],PLocalFitParams[[Mnr,5]]],
  {yg,PMarkers[[Mnr,2]]*PResolution,(PMarkers[[Mnr,2]]+PMarkers[[Mnr,3]])*PResolution},
  PlotStyle->Hue[Mnr/Length[PMarkers]],PlotRange->All],{Mnr,Length[PMarkers]}];
TrueCenters=Table[Plot[(yg-TruePoints[[Mnr,2]]*TResolution)*1000,{yg,(TruePoints[[Mnr,2]]-
  TMarkers[[Mnr,3]]/2)*TResolution,(TruePoints[[Mnr,2]]+TMarkers[[Mnr,3]]/2)*TResolution},
  PlotStyle->Directive[Hue[Mnr/Length[TruePoints]],Dashed],
  PlotRange->{0,1}],{Mnr,Length[TruePoints]}];
FIONAFits=Table[Plot[Gauss2D[yg,TPoints[[Mnr,2]]*TResolution,(TMarkers[[Mnr,2]]+

PLocalFitParams[[Mnr,2]])*TResolution,TPoints[[Mnr,2]]*TResolution,1/PPoints[[Mnr,3]]*TResolution,
  PLocalFitParams[[Mnr,4]],PLocalFitParams[[Mnr,5]]],{yg,(TMarkers[[Mnr,2]]+PC)*TResolution,
  (TMarkers[[Mnr,2]]+TMarkers[[Mnr,3]]+PC)*TResolution},PlotStyle->Hue[Mnr/Length[TMarkers]],
  PlotRange->{{(TMarkers[[Mnr,2]]+PC)*TResolution,(TMarkers[[Mnr,2]]+TMarkers[[Mnr,3]]+
  PC)*TResolution},All}],{Mnr,Length[TMarkers]}];
(* Slope 1000 = almost vertical;-) *)
FIONACenters=Table[Plot[(yg-(TMarkers[[Mnr,2]]+PLocalFitParams[[Mnr,2]])*TResolution)*1000,
  {yg,(TMarkers[[Mnr,2]]+PC)*TResolution,(TMarkers[[Mnr,2]]+TMarkers[[Mnr,3]]+PC)*TResolution},
  PlotStyle->Directive[Hue[Mnr/Length[TMarkers]]],PlotRange->{0,1.1}],{Mnr,Length[TMarkers]}];
```

```
(* Output as Lists *)
Print["Tracking of the fluorescent centers:"];
Table[{Mnr,Show[FIONASections[[Mnr]],FIONATrack[[Mnr]]]},{Mnr,Length[FIONASections]}]

(* No "TruePositions" for experimental data *)
(* Calculation of distance = quick'n'dirty, only scaled by 1/2 trace of TransformationMatrx *)
(* Just for quicly checking the result. *)
Print[{"# ","Distance between lines ","Image: AFM dotted, True Position dashed,
  FIONA (with center marked) stroke"}];
If[AutomaticAnalysis,
  Print[Table[{Mnr,Abs[TMarkers[[Mnr,2]]+PLocalFitParams[[Mnr,2]]-TPoints[[Mnr,2]]]*TResolution,
    Show[AFMSections[[Mnr]],TrueCenters[[Mnr]],FIONAFits[[Mnr]],FIONACenters[[Mnr]]]},
      {Mnr,Length[TMarkers]}]],Print[Table[{Mnr,Abs[TMarkers[[Mnr,2]]+PLocalFitParams[[Mnr,2]]-
      TPoints[[Mnr,2]]]*TResolution,
    Show[AFMSections[[Mnr]],FIONAFits[[Mnr]],FIONACenters[[Mnr]],
      PlotRange->All]},{Mnr,Length[TMarkers]}]]
  ];
Tracking of the fluorescent centers:
```

{# , Image: AFM dotted, True Position dashed, FIONA (with center marked) stroke}

{{1,   },

{2,   },

{3,   },

{4,   },

{5   }}
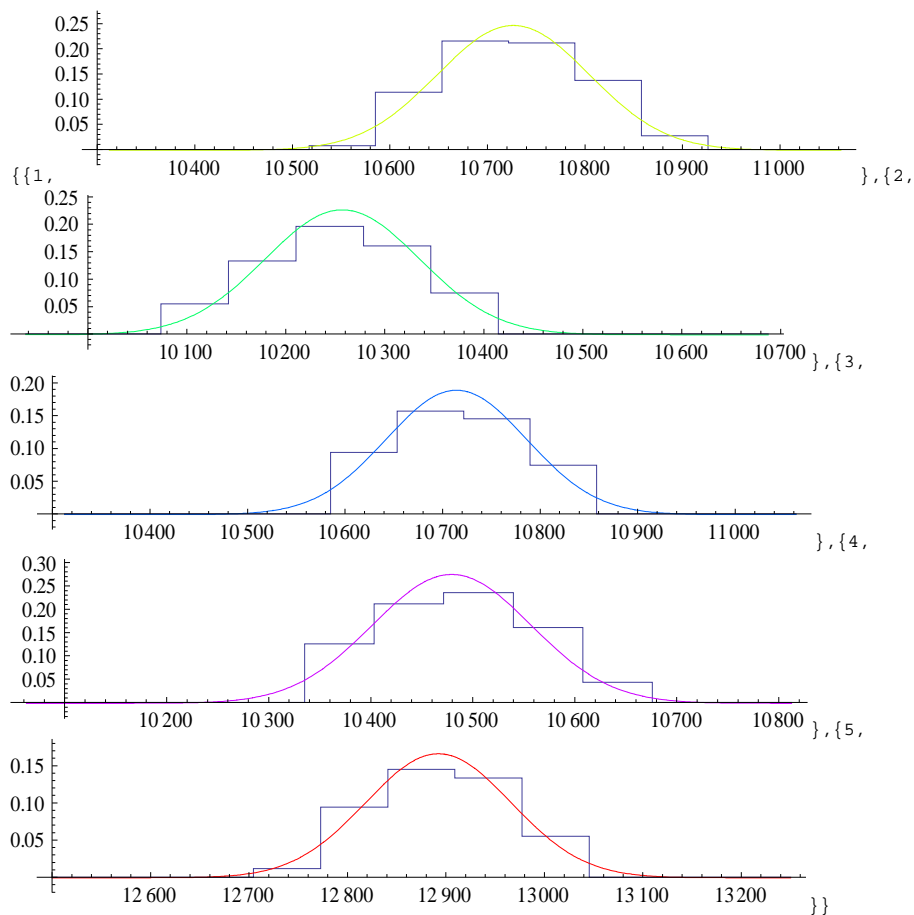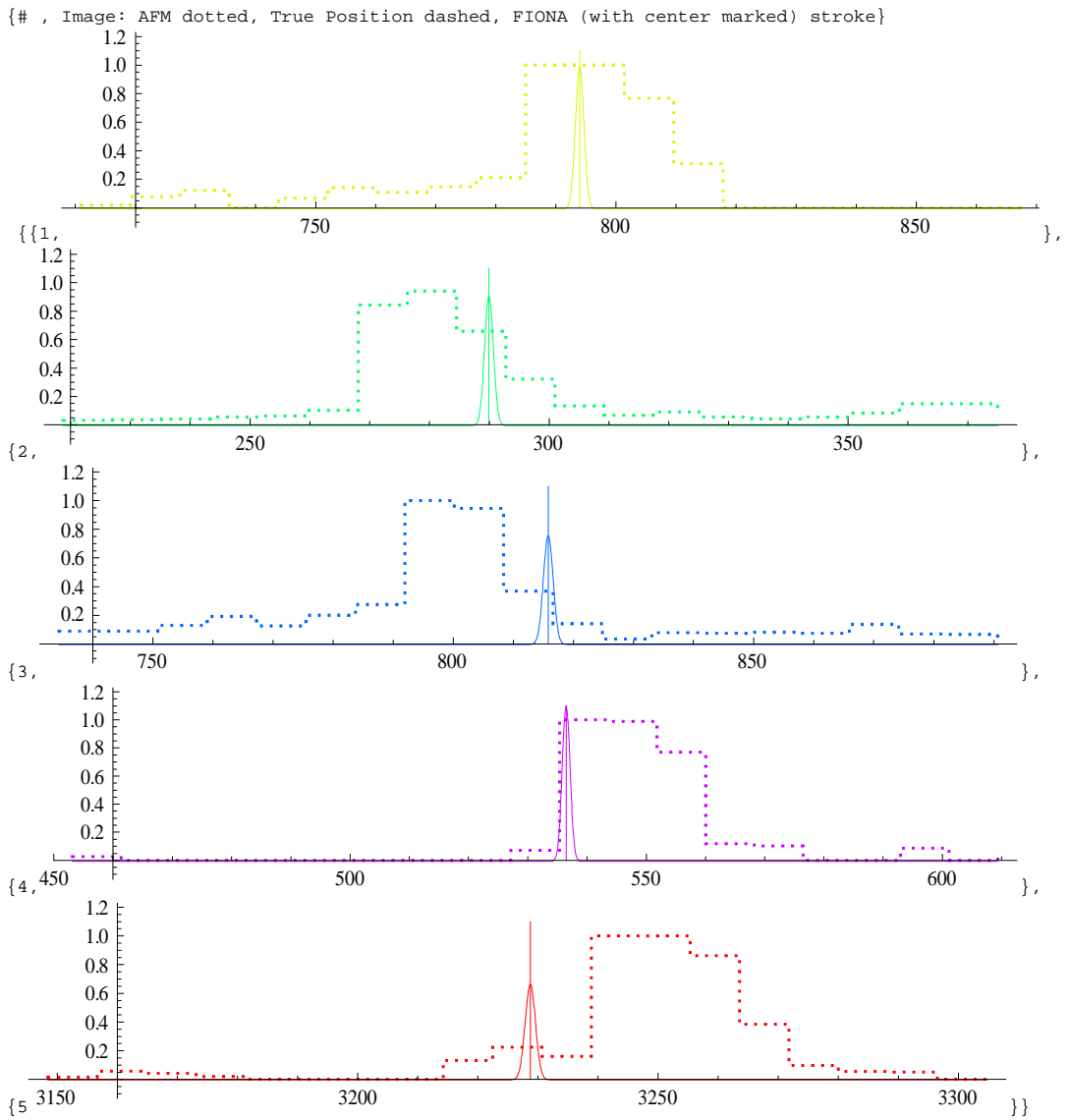
```
(* Write Collected Results to text file *)
Export["CollectedResults.txt",StringReplace[ToString[MatrixForm[CollectedResults,
  TableSpacing->{0,1}]],{"{"|"}"->"",", "->"\t"}],"CSV"]
Export["CollectedCoordinates.txt",CollectedCoordinates,"CSV"]
 CollectedResults.txt
 CollectedCoordinates.txt
```

A.4. Image simulation code

The code for generating simulated images (unchanged running version).

```
1   (***********************************)
2   (*      Image Generation v0.9.4       *)
3   (* Calculate many images overnight *)
4   (***********************************)
5
6   (* Poissonian Noise generation function, cut-off at 0 *)
7   PNoise[RealValue_] := If[Round[RealValue]<=0, 0,
8    RandomInteger[PoissonDistribution[Round[RealValue]]]];
9   SetAttributes[PNoise, Listable];
10
11  (* Valid only for convex polygons! *)
12  (* from: "An Efficient Test for a Point to Be in a Convex Polygon", *)
13  (* Wolfram Demonstrations Project:
14   http://demonstrations.wolfram.com/AnEfficientTestForAPointToBeInAConvexPolygon/ *)
15  area2[pts_] := Total[pts (pts // RotateRight[{{0, -1}, {1, 0}}.# & /@ #] &), 2]/2;
16  angtest[p1_, p2_] := p1.{{0, -1}, {1, 0}}.p2 > 0;
17  InsideQ[PointPosition_, Corners_] := Corners // # - PointPosition & /@ # & //
18   {#, RotateLeft@#} & // Transpose // angtest @@ # & /@ # & // Equal @@ # &
19
20  (* Initialization Values *)
21  SimFileOutputBase = "df_sim01_";
22  SimImageSize = {512, 512};
23  ScaleFactor = 4.0;
24  SimAFMSize = {512, 512};
25  ImageRatio = SimAFMSize[[1]]/SimImageSize[[1]];
26
27  MaxHeight = 255;
28  EMGainMax = 1000; FullWellCapacity = 370000; AnalogGain = 5;
29  (* As typically adjusted by hand: Max = 90% white *)
30  EMGainRelative =  Round[MaxHeight / (MaxPhotons / FullWellCapacity *
31   MaxHeight / 255* EMGainMax * AnalogGain)] * 0.9;
32  CountsPerPhoton = MaxHeight / FullWellCapacity * EMGainRelative /
33   255 * EMGainMax * AnalogGain;
34
35  PeakForm[x_, y_, mx_, my_, std_, zmax_] =
36   zmax*Exp[-((x - mx)^2)/2/std]*Exp[-((y - my)^2)/2/std];
37
38  (* Big loop starts here, and runs once for each image pair *)
39  For[ImageNr = 1, ImageNr <= 50, ImageNr++,
40   FileNameBase = SimFileOutputBase <> IntegerString[ImageNr, 10, 3];
41   VainCounter = 0;
42   Label[StartLoop];
43   If[VainCounter > 7, Print["Check your settings! Not enough good ",
44    "points! Exit!"]; Break[];];
45   (* New image parameters *)
46   BackgroundNoise = Random[Integer,{2,40}];
47   (*BackgroundNoise = 3;*)
48   (* Width of the optical peaks (in pixel units) *)
49   (*PeakWidth = Random[Real, {2, 8}];*)
50   PeakWidth = 3.5;
51   MaxPhotons = 800;
```

```
52
53   (* Offset and transformation matrix *)
54    SOffset = Table [Random [Real,
55     {-SimImageSize [[1]]/10, SimImageSize [[1]]/10}], {2}];
56   (* Random, but not too heavy distortions *)
57    PlainSMatrix = {{Random [Real, {0.95, 1.05}], Random [Real, {-0.05, 0.05}]},
58     {Random [Real, {-0.05, 0.05}], Random [Real, {0.95, 1.05}]}};
59    SMatrix = PlainSMatrix / ScaleFactor;
60
61   (* Take a radom number of random positions (away from the edges) *)
62   (* -> Pixel coordinates in FIONA image *)
63    RandomPos =
64     Table [{Random [Real, {2*PeakWidth, SimImageSize [[1]] - 2*PeakWidth}],
65      Random [Real, {2*PeakWidth, SimImageSize [[2]] - 2*PeakWidth}]},
66     {Mnr, Random [Integer, {60, 90}]}];
67
68   (* Only points in the AFM image area of of the FIONA image will show up *)
69    ImgOffset = {SimImageSize [[1]]/2 * (1 - 1/ScaleFactor),
70     SimImageSize [[2]]/2 * (1 - 1/ScaleFactor)};
71    ImgCorners = {SMatrix.{0,0} + ImgOffset + SOffset,
72     SMatrix.{SimImageSize [[1]],0} + ImgOffset + SOffset,
73     SMatrix.SimImageSize + ImgOffset + SOffset,
74     SMatrix.{0,SimImageSize [[2]]} + ImgOffset + SOffset};
75     GoodPos = Select [RandomPos, InsideQ [#[[1;;2]], ImgCorners]&];
76
77   (* Stop if not enough points *)
78    If[Length [GoodPos] <= 4, VainCounter++; Goto [StartLoop];];
79
80   (* Fake AFM image (at inversely transformed positions) *)
81   (* (+point in lower right corner for easier output)    *)
82   (* Coordinates corrected by offset (select center region) plus *)
83   (* scaled by the zoom and, if applicable, the pixel resolution *)
84    InverseSMatrix = Inverse [SMatrix];
85    SimAFMData = SparseArray [Append [Round [
86     Table [InverseSMatrix.(GoodPos [[Pnr, 1;;2]] - ImgOffset - SOffset), {Pnr,
87      Length [GoodPos]}]], SimAFMSize] -> ConstantArray [255, {Length [GoodPos]+1}]];
88
89   (* No Noise added for AFM (useless for local max. tracker) *)
90   (* Output 1: AFM *)
91    Export [FileNameBase <> "T.tif", Normal [Transpose [SimAFMData]],
92     "Data", ImageSize -> SimAFMSize];
93
94   (* Output 2: Info-File *)
95    InfoFile = OpenWrite [FileNameBase <> "I.txt"];
96    WriteString [InfoFile, "(* Info for File: ", FileNameBase, " *)\n",
97     "NPeaks = ", Length [GoodPos], ";\nTruePoints = ",
98     Table [InverseSMatrix.(GoodPos [[Pnr, 1;;2]] - ImgOffset - SOffset),
99     {Pnr, Length [GoodPos]}],";\n",
100    "TMarkers = Transpose [Append [Transpose [Round [TruePoints -12]],",
101    "Table [24,{Length [TruePoints]}]]];\n", "BackGroundNoise = ",
102    BackgroundNoise, ";\n", "PeakWidth = ", PeakWidth,
103    ";\nTrueTransM = ", SMatrix, ";\nTrueTransO = ", SOffset + ImgOffset,
104    ";\nTruePPoints = ", GoodPos, ";\n", "PMarkers = TruePPoints;\n",
105    "PMarkers = Transpose [Append [Transpose [Round [PMarkers -12]],",
106    "Table [24,{Length [PMarkers]}]]];", "\nTResolution = ",
```

```
107    (60.5/ScaleFactor/2), ";\nPResolution = 60.5;\nEMGainRelative = ",
108    EMGainRelative,"\nMaxPhotons = ",MaxPhotons, ";\nBadPoints = {};",
109    "\nBMarker = {1,1,30};\n"];
110   Close[InfoFile];
111
112  (* Create Peaks at selected random positions in FIONA image *)
113   SimImageData = ConstantArray[BackgroundNoise,SimImageSize];
114   SimImageData = SimImageData + Array[(Sum[Chop[
115    Round[PeakForm[#1, #2, RandomPos[[Pnr,1]], RandomPos[[Pnr,2]],
116    PeakWidth, MaxPhotons]]], {Pnr,Length[RandomPos]}]) &, SimImageSize];
117
118  (* Transform into greyscale values, add noise, cutoff at "white" *)
119   SimImageData = Clip[Round[PNoise[SimImageData] * CountsPerPhoton], {0,MaxHeight}];
120
121  (* Output 3: Optics *)
122   Export[FileNameBase <> "P.tif", Transpose[SimImageData], "Data",
123    ImageSize -> SimImageSize];
124
125   Print["File ", ImageNr, " done."];
126  ];(* End of big loop *)
127  Print["Finished!"];
```

This code produces two image files as described in section 4.4.2, plus a plain text file containing all the relevant information. The format of this file is designed to be easily parseable by *Mathematica* for later analysis. A sample file is shown below:

```
1  (* Info for File: df_simN01_001 *)
2  NPeaks = 9;
3  TruePoints = {{178.424, 28.6411}, {182.372, 228.655}, {191.587, 32.3746},
4   {379.173, 102.64}, {280.058, 241.015}, {109.626, 31.6879},
5   {135.708, 105.239}, {410.85, 208.62}, {397.341, 131.561}};
6  TMarkers = Transpose[Append[Transpose[Round[TruePoints-12]],
7   Table[24,{Length[TruePoints]}]]];
8  BackGroundNoise = 2;
9  PeakWidth = 3;
10 TrueTransM = {{0.258296, -0.010476}, {0.00195416, 0.240354}};
11 TrueTransO = {224.339, 141.642};
12 TruePPoints = {{270.125, 148.875}, {269.05, 196.957}, {273.486, 149.798},
13  {321.203, 167.053}, {294.152, 200.119}, {252.323, 149.473},
14  {258.29, 167.202}, {328.275, 192.588}, {325.593, 174.04}};
15 PMarkers = TruePPoints;
16 PMarkers = Transpose[Append[Transpose[Round[PMarkers-12]],
17  Table[24,{Length[PMarkers]}]]];
18 TResolution = 7.5625;
19 PResolution = 60.5;
20 EMGainRelative = 17.1;
21 MaxPhotons = 800;
22 BMarker = {1,1,30};
23 BadPoints = {};
```

.

Selbstständigkeitserklärung

Hiermit erkläre ich, dass ich diese Arbeit in allen Teilen selbstständig verfasst und keine anderen als die in der Arbeit angegebenen Hilfsmittel benutzt habe. Soweit wörtlich oder sinngemäß Inhalte aus anderen Quellen entnommen wurden, ist dies ausdrücklich kenntlich gemacht. Zeichnungen, Diagramme und bildliche Darstellungen habe ich, soweit nicht anderes angegeben, selbst gefertigt.

Würzburg, 30. September 2009
 David Fronczek